Effects of mixture composition and turbulence intensity on flame front structure and burning velocities of premixed turbulent hydrocarbon/air Bunsen flames

Parsa Tamadonfar*, Ömer L. Gülder

Institute for Aerospace Studies, University of Toronto, 4925 Dufferin Street, Toronto, Ontario M3H 5T6, Canada

ABSTRACT

The influences of the equivalence ratio, turbulence intensity, and different thermo-diffusive characteristics on the flame brush characteristics, instantaneous flame front structures, and burning velocities of premixed turbulent methane/–, ethane/–, and propane/air Bunsen flames were investigated systematically. Particle image velocimetry and Mie scattering techniques were utilized to measure the turbulence statistics and to visualize flame front corrugations, respectively. All experiments were performed under a constant bulk flow velocity of 21.0 m/s. The equivalence ratio range was from 0.7 to 1.35 for methane/air flames, 0.7–1.45 for ethane/air flames, and 0.8–1.35 for propane/air flames. Two perforated plates were used to produce different turbulence levels. A series of comprehensive parameters including the characteristic flame height, mean flame brush thickness, mean volume of the turbulent flame region, mean fuel consumption rate, two-dimensional flame front curvature, local flame front angle, two-dimensional flame surface density, wrinkled flame surface area, turbulent burning velocity, mean flamelet consumption velocity, and mean turbulent flame stretch factor were obtained. The mean turbulent flame stretch factor displayed a dependence on the equivalence ratio and turbulence intensity. Results show that the mean turbulent flame stretch factors for lean/stoichiometric and rich mixtures were not equal when the unstrained premixed laminar burning velocity, non-dimensional bulk flow velocity, non-dimensional turbulence intensity, and non-dimensional longitudinal integral length scale were kept constant.

© 2015 The Combustion Institute. Published by Elsevier Inc. All rights reserved.

1. Introduction

For the improvement of certain class of combustion devices such as the lean premixed gas-turbines for power generation and the homogeneous charge spark-ignition engines for transportation, we need a better understanding of premixed turbulent combustion [1]. Despite the continuing progress in the field of premixed turbulent combustion, there still exist many unresolved problems regarding the underlying physics of the associated processes. The knowledge of flame brush characteristics, instantaneous flame front structures, and burning velocities, which are the manifestations of turbulence–flame interactions, is necessary in order to understand the mechanism behind the premixed turbulent combustion. This kind of information is not only desired for a better design of the related combustion devices but also for the numerical model testing.

The premixed turbulent flame geometries are classified into the "Envelope" category (Bunsen-type flames), "Oblique" category (V-shaped flames), "Unattached" category (counterflow and swirl-stabilized flames), and propagating flame kernels [2–4]. Abdel-Gayed and Bradley [5] examined a large number of burning velocity data sets for premixed turbulent flames on different burners, extracted from different sources. They also developed a two-eddy theory of burning, and they compared it with experimentally measured values. They suggested that the ratio of the turbulent to the laminar burning velocity might be correlated with the ratio of the root-mean-square (r.m.s.) of velocity fluctuations to the unstrained premixed laminar burning velocity and with the cold gas turbulent Reynolds number. Later, Abdel-Gayed et al. [6] modified the two-eddy theory of burning proposed in [5] to estimate the effect of flame straining on the burning velocity, and they reported burning velocity values obtained in an explosion bomb. They showed that the turbulent burning velocity increases with increasing r.m.s. of velocity fluctuations, whereas by further increasing the latter property, the rate of increase of the burning velocity with the r.m.s. of velocity fluctuations decreases. This observation is called the "bending" phenomenon [7]. Similar trends were previously reported in the literature, see, for example, Sokolik et al. [8], Karpov and Severin [9], Bradley [10], Duclos et al. [11], Aldredge et al. [12], Peters [13], Shy et al. [14], Kido et al. [15], Kobayashi et al.

* Corresponding author.
  E-mail addresses: tamadonfar@utias.utoronto.ca, parsa.tamadonfar@utoronto.ca
 (P. Tamadonfar).

[16], Filatyev et al. [3], and Fairweather et al. [17]. This phenomenon may be attributed to the flamelets merging along with the gas expansion [3]. Abdel-Gayed et al. [6] presented the ratio of the turbulent to the laminar burning velocity in terms of the parameters previously reported in [5] plus a Lewis number for the deficient reactant and the dimensionless activation energy. Experimental measurements showed that the burning velocity of premixed turbulent flames increases with decreasing Lewis number for the deficient reactant, see, for example, Karpov and Severin [9], Kido et al. [15,18], and Nakahara et al. [19]. Abdel-Gayed et al. [20] presented the ratio of the turbulent to the laminar burning velocity in terms of the ratio of the effective r.m.s. of velocity fluctuations to the unstrained premixed laminar burning velocity and the Karlovitz flame stretch factor. Bradley [10] showed that the ratio of the turbulent burning velocity to the effective r.m.s. of velocity fluctuations has a power law relation to the product of the Karlovitz flame stretch factor and the Lewis number by investigating the experimental values reported in [20]. Gülder [21] proposed conceptual models for the prediction of burning velocity for three different combustion regimes. Each model was tested by comparing it to the measured data of various experimental rigs. It should be emphasized that all of these models are in terms of the turbulence statistics, namely the r.m.s. of velocity fluctuations and turbulent length scale. In their comprehensive review papers, Lipatnikov and Chomiak [22,23] reviewed the available empirical correlations to represent the turbulent burning velocity in the literature, and they discussed the effects of various parameters such as the turbulence intensity, turbulent length scale, unstrained premixed laminar burning velocity, molecular heat diffusivity, pressure, and Lewis number for the deficient reactant on the burning velocity of premixed turbulent flames.

Many attempts have been made over several decades in order to correlate the measured turbulent burning velocity data in terms of different parameters such as the turbulent length scale, turbulent Reynolds number, laminar flame thickness, volumetric expansion ratio, and the effects of non-unity Lewis number [4]. As noted in Bilger et al. [4], the correlations available in the literature are limited, and they are sensitive to flow configuration. It is proposed in [4,7] that the turbulent burning velocity data of one flame category should only be used for a geometry-specific correlation, and they should not be utilized for other flame categories. Filatyev et al. [3] stated that the turbulence intensity and turbulent length scale cannot be solely used for constructing a correlation to represent the turbulent burning velocity for Bunsen-type flames. This necessitated additional parameters for the turbulent burning velocity correlation, namely the bulk flow velocity, burner width, and turbulent Markstein number. Tamadonfar and Gülder [24] showed that the turbulent burning velocity decreases with increasing bulk flow velocity when other turbulence statistics are kept constant. They stated that this observation may be attributed to the formation of local extinctions due to an increase of flame front stretching caused by the large velocity gradients in shear layers. In their comprehensive study, Daniele et al. [25] evaluated the thermo-diffusive characteristics of flames stabilized on an axisymmetric burner by measuring the mean turbulent Markstein number using a fractal method. They showed that the mean turbulent Markstein number decreases with increasing equivalence ratio for lean syngas/air flames. In addition, the mean turbulent Markstein numbers for pure methane/air mixtures are equal to zero, and their absolute values increase for hydrogen-containing fuels with increasing H_2 content [25]. The physical mechanism associated with the thermo-diffusive effects is thoroughly explained by Lipatnikov and Chomiak [23]. In this mechanism, the flamelet consumption velocity increases (decreases) locally due to the local variations in enthalpy and mixture composition. Following Lipatnikov and Chomiak [23], if the mass diffusivity of the deficient reactant is larger than the thermal diffusivity of the mixture or the mass diffusivity of the excess reactant, the chemical energy provided to the flame front which

Table 1
Summary of geometrical properties and upstream position of the perforated plate from the burner exit for each of the perforated plate used in this study. Symbols: d = hole diameter of the perforated plate; M = mesh size of the perforated plate; β = blockage ratio of the perforated plate; h_e = upstream position of the perforated plate from the burner exit.

Perforated plate	d (mm)	M (mm)	β (%)	h_e (mm)
TG-I	1.0	1.3	53	100.1
TG-II	0.9	1.3	62	44.5

is convex toward the reactants surpasses the heat losses due to the molecular conductivity, or the mixture composition for the lean mixture leads to the stoichiometric mixture due to the faster diffusion of the deficient reactant compared to the excess reactant. This process results in an increase of the local flamelet consumption velocity. On the other hand, the opposite phenomena occur for the flame front which is concave toward the reactants. This results in the faster propagation of the flame front which is convex toward the reactants and the slower propagation of the flame front which is concave toward the reactants. Thus, the flame wrinkling grows. To the best of the authors' knowledge, there has not been any systematic investigation conducted on evaluating the mean flamelet consumption velocity using the flame surface density method when other turbulence statistics are kept constant.

In this study, we explore the effects of the equivalence ratio, turbulence intensity, and different thermo-diffusive characteristics on the flame brush characteristics, instantaneous flame front structures, and burning velocities of premixed turbulent methane/–, ethane/–, and propane/air Bunsen flames. A series of broad parameters including the characteristic flame height, mean flame brush thickness, mean volume of the turbulent flame region, mean fuel consumption rate, two-dimensional flame front curvature, local flame front angle, two-dimensional flame surface density, wrinkled flame surface area, turbulent burning velocity, mean flamelet consumption velocity, and mean turbulent flame stretch factor were evaluated from the experimental data.

2. Experimental methodology

2.1. Bunsen-type burner

An axisymmetric Bunsen-type burner with a nozzle inner diameter, D, of 11.1 mm was utilized to produce premixed turbulent flames. The geometry of its components was documented in detail in [26]. The calibrated mass flow meters were used to control the flow rates of the filtered air and fuel. The accuracy for each of the flow meter was ±0.80% on its reading, and ±0.20% on its full scale. Three different hydrocarbons (methane, ethane, and propane) were utilized as the fuel in the experiments. The flame was anchored to the rim of the burner using an annular premixed ethylene/air pilot flame. Two perforated plates, that is, TG-I and TG-II, were used independently in order to generate different turbulence levels. Each of the perforated plate was mounted upstream of the burner exit. The holes of the perforated plates are arranged in a hexagonal array. This method of turbulence generation has been extensively utilized in the literature, see, for example, [24,27–37]. The hole diameter (d), mesh size (M), blockage ratio (β), and upstream position of the perforated plate from the burner exit (h_e) for each of the perforated plate are summarized in Table 1. The time-averaged image of a luminosity for a representative flame condition, Flame M12, is shown in Fig. 1.

2.2. Flow field characterization and test conditions

The two-dimensional particle image velocimetry was utilized to measure the instantaneous velocity vectors. The light source which
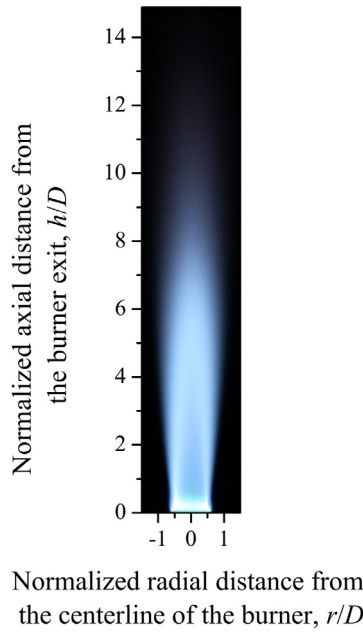
Fig. 1. Time-averaged image of a luminosity for Flame M12, where r is the radial distance from the centerline of the burner, and h is the axial distance from the burner exit. Table 2 summarizes the characteristics of this flame condition. This image was captured using a color digital camera.

Fig. 2. (a) and (b) show the contour plots of the mean axial velocity and mean radial velocity when TG-I was utilized for turbulence production. (c) and (d) show the contour plots of the mean axial velocity and mean radial velocity when TG-II was used for turbulence production. These experiments were performed under non-reacting conditions.

was used for illuminating the seeding particles in the flow field was a double-pulsed Nd:YAG laser (Litron, Nano-L, 200-15) with a maximum output energy and wavelength of 200 mJ/pulse and 532 nm, respectively. The seeding particles were produced by atomizing olive oil to sub-micron droplets using a nebulizer. A similar technique has been previously used in the literature, see, for example, [24,27,33–37]. The laser beam was converted into a laser sheet using a LaVision light sheet optical assembly. It consists of two spherical lenses, $f = +85$ and -75 mm, and one cylindrical lens, $f = -20$ mm, where f is the focal length of the lens. This optical assembly results in a laser sheet of approximately 300 μm at full-width-at-half-maximum (FWHM). The experimental images were captured using a LaVision Imager pro X camera with a resolution of 2048×2048 pixels^2. A Sigma macro lens with a focal length of 105 mm operating at $f/8.0$ was mounted on the camera in order to collect the scattered light from the seeding particles. The field-of-view captured by the current system is approximately 56×56 mm^2. A 532 nm bandpass filter was located in front of the lens to decrease the interference of unsought wavelengths from the environment on the camera's CCD. The DaVis 7.2 software provided by LaVision was used to calculate the velocity components in the axial and radial directions. The camera was calibrated using a three-dimensional calibration plate. This procedure ensures that the location of the measurement plane is accurately mapped on the camera's CCD. Five hundred image pairs were captured under the non-reacting condition at a frequency of 6 Hz for each experimental condition. A multi-pass vector estimation algorithm was implemented on each image pair with interrogation box sizes decreasing from 64×64 to 32×32 pixels^2 with a 50% overlap. This resulted in a resolution and vector spacing of 880 and 440 μm, respectively. The time delay between consecutive laser pulses in order to capture an image pair was adjusted to ensure that the displacement of seeding particles was less than a quarter of the final interrogation box size.

Six sets of experiments were performed in this study. Conditions of these six sets comprising 44 flames are tabulated in Table 2. The bulk flow velocity, U_B, which was determined by the total volumetric flow rate was equal to 21.0 m/s for all flame conditions. The contour plots of the mean axial velocity, $\langle U \rangle$, and mean radial velocity, $\langle V \rangle$, for
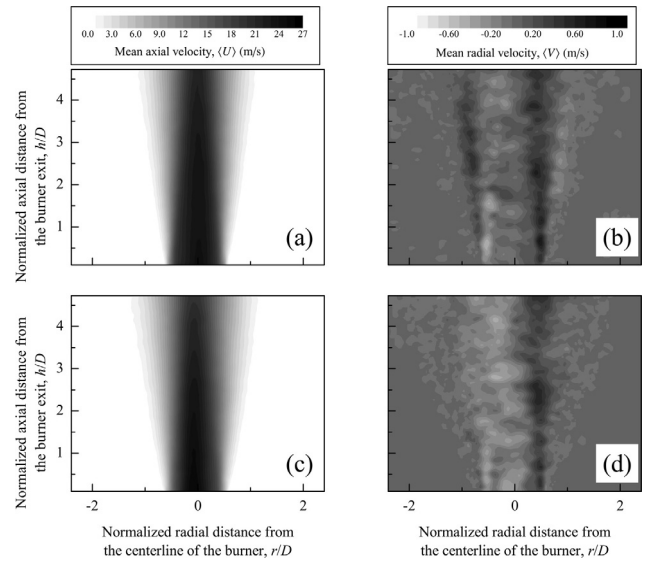
the conditions when TG-I and TG-II were utilized for turbulence production are shown in Fig. 2(a)–(d), where $\langle \rangle$ determines an average of the investigated property. It is observed that the mean flow spreads out with increasing normalized axial distance from the burner exit, as observed previously, see, for example, Mi et al. [38]. Furthermore, the profiles of the mean axial velocity and mean radial velocity normalized by the bulk flow velocity with respect to the normalized radial distance from the centerline of the burner, r/D, at $h/D = 0.5$ are shown in Fig. 3(a) and (b), respectively, where r is the radial distance from the centerline of the burner, and h is the axial distance from the burner exit. The mean axial velocity profile is approximately similar to a top-hat profile when TG-I is mounted at $h_e = 100.1$ mm, and it resembles to a parabolic profile when TG-II is mounted at $h_e = 44.5$ mm. The latter observation may be attributed to the coalition of turbulent jets produced by the holes of the perforated plate. Chen and Bilger [28] showed a similar trend in their experimental measurements. Results show a relatively low radial velocity with its maximum near the tip of the burner. The turbulence for the first, third, and fifth sets of experiments was generated using TG-I, whereas TG-II was utilized for other sets of experiments. The equivalence ratio, ϕ, was changed from 0.7 to 1.35 for methane/air flames (Flames M1–M8 and M9–M16), 0.7–1.45 for ethane/air flames (Flames E1–E8 and E9–E16), and 0.8–1.35 for propane/air flames (Flames P1–P6 and P7–P12).

The total turbulence intensity, u', is an important parameter in the flame/flow interactions. This property is controlled by the geometry and upstream location of the turbulence generator from the burner exit [24,30,31]. The r.m.s. of velocity fluctuations in the radial direction, $\langle v^2 \rangle^{1/2}$, was assumed to be equal to the r.m.s. of velocity fluctuations in the azimuthal direction, $\langle w^2 \rangle^{1/2}$, due to the axisymmetric nature of the flow for the Bunsen-type burner. Therefore, the r.m.s. of velocity fluctuations in the axial, $\langle u^2 \rangle^{1/2}$, and radial, $\langle v^2 \rangle^{1/2}$, directions were utilized to determine the total turbulence intensity using the following formula:

$$u' = \left(\frac{\langle u^2 \rangle + \langle v^2 \rangle + \langle w^2 \rangle}{3} \right)^{\frac{1}{2}} = \left(\frac{\langle u^2 \rangle + 2\langle v^2 \rangle}{3} \right)^{\frac{1}{2}}. \tag{1}$$

The r.m.s. of velocity fluctuations in the axial and radial directions as well as the total values normalized by the bulk flow velocity with respect to the normalized radial distance from the centerline of the

Table 2
Summary of experimental conditions. Symbols: ϕ = equivalence ratio; U_B = bulk flow velocity; u' = total turbulence intensity; S_L^0 = unstrained premixed laminar burning velocity; Λ_L = longitudinal integral length scale; δ_f = Zel'dovich thickness; Re_{Λ_L} = turbulent Reynolds number; Ka = turbulent Karlovitz number; Da = turbulent Damköhler number; Sc = Schmidt number.

| Set of exp.	Flame	ϕ (–)	U_B (m/s)	u' (m/s)	S_L^0 (m/s)	Λ_L (mm)	δ_f (mm)	U_B/S_L^0 (–)	u'/S_L^0 (–)	Λ_L/δ_f (–)	u'/U_B (%)	Re_{Λ_L} (–)	Ka (–)	Da (–)	Sc (–)
I	M1	0.7	21.0	0.91	0.198	2.39	0.110	105.7	4.6	21.8	4.3	138	3.4	4.8	0.72
	M2	0.8	21.0	0.91	0.279	2.39	0.078	75.1	3.3	30.6	4.3	138	1.7	9.4	0.72
	M3	0.9	21.0	0.91	0.345	2.39	0.063	60.7	2.6	37.9	4.3	138	1.1	14.4	0.72
	M4	1.0	21.0	0.91	0.386	2.39	0.056	54.3	2.4	42.4	4.3	138	0.9	18.0	0.72
	M5	1.1	21.0	0.91	0.384	2.39	0.057	54.6	2.4	42.2	4.3	138	0.9	17.8	0.72
	M6	1.2	21.0	0.91	0.341	2.39	0.064	61.5	2.7	37.5	4.3	138	1.2	14.1	0.72
	M7	1.25	21.0	0.91	0.293	2.39	0.074	71.6	3.1	32.2	4.3	138	1.6	10.4	0.72
	M8	1.35	21.0	0.91	0.181	2.39	0.120	115.6	5.0	19.9	4.3	138	4.1	4.0	0.72
II	M9	0.7	21.0	1.89	0.198	2.64	0.110	105.7	9.5	24.1	9.0	316	9.7	2.5	0.72
	M10	0.8	21.0	1.89	0.279	2.64	0.078	75.1	6.8	33.8	9.0	316	4.9	5.0	0.72
	M11	0.9	21.0	1.89	0.345	2.64	0.063	60.7	5.5	41.9	9.0	316	3.2	7.7	0.72
	M12	1.0	21.0	1.89	0.386	2.64	0.056	54.3	4.9	46.8	9.0	316	2.6	9.6	0.72
	M13	1.1	21.0	1.89	0.384	2.64	0.057	54.6	4.9	46.6	9.0	316	2.6	9.5	0.72
	M14	1.2	21.0	1.89	0.341	2.64	0.064	61.5	5.5	41.4	9.0	316	3.3	7.5	0.72
	M15	1.25	21.0	1.89	0.293	2.64	0.074	71.6	6.4	35.5	9.0	316	4.4	5.5	0.72
	M16	1.35	21.0	1.89	0.181	2.64	0.120	115.6	10.4	22.0	9.0	316	11.6	2.1	0.72
III	E1	0.7	21.0	0.91	0.238	2.39	0.060	88.2	3.8	39.5	4.3	144	1.1	10.3	1.05
	E2	0.8	21.0	0.91	0.325	2.39	0.044	64.5	2.8	54.1	4.3	144	0.6	19.4	1.05
	E3	0.9	21.0	0.91	0.390	2.39	0.037	53.7	2.3	64.8	4.3	144	0.4	27.8	1.05
	E4	1.0	21.0	0.91	0.430	2.39	0.033	48.8	2.1	71.5	4.3	144	0.3	33.8	1.05
	E5	1.15	21.0	0.91	0.434	2.39	0.033	48.3	2.1	72.2	4.3	144	0.3	34.5	1.05
	E6	1.25	21.0	0.91	0.387	2.39	0.037	54.2	2.3	64.3	4.3	144	0.4	27.4	1.05
	E7	1.35	21.0	0.91	0.305	2.39	0.047	68.7	3.0	50.8	4.3	144	0.7	17.1	1.05
	E8	1.45	21.0	0.91	0.218	2.39	0.066	95.9	4.2	36.3	4.3	144	1.3	8.7	1.05
IV	E9	0.7	21.0	1.89	0.238	2.64	0.060	88.2	7.9	43.7	9.0	330	3.2	5.5	1.05
	E10	0.8	21.0	1.89	0.325	2.64	0.044	64.5	5.8	59.7	9.0	330	1.7	10.3	1.05
	E11	0.9	21.0	1.89	0.390	2.64	0.037	53.7	4.8	71.6	9.0	330	1.2	14.8	1.05
	E12	1.0	21.0	1.89	0.430	2.64	0.033	48.8	4.4	78.9	9.0	330	1.0	18.0	1.05
	E13	1.15	21.0	1.89	0.434	2.64	0.033	48.3	4.3	79.7	9.0	330	0.9	18.3	1.05
	E14	1.25	21.0	1.89	0.387	2.64	0.037	54.2	4.9	71.0	9.0	330	1.2	14.6	1.05
	E15	1.35	21.0	1.89	0.305	2.64	0.047	68.7	6.2	56.1	9.0	330	1.9	9.1	1.05
	E16	1.45	21.0	1.89	0.218	2.64	0.066	95.9	8.6	40.1	9.0	330	3.7	4.6	1.05
V	P1	0.8	21.0	0.91	0.284	2.39	0.040	73.8	3.2	59.1	4.3	149	0.5	18.5	1.26
	P2	0.9	21.0	0.91	0.356	2.39	0.032	59.0	2.6	74.0	4.3	149	0.3	28.9	1.26
	P3	1.0	21.0	0.91	0.394	2.39	0.029	53.2	2.3	82.0	4.3	149	0.3	35.5	1.26
	P4	1.15	21.0	0.91	0.398	2.39	0.029	52.7	2.3	82.8	4.3	149	0.3	36.2	1.26
	P5	1.25	21.0	0.91	0.360	2.39	0.032	58.2	2.5	74.9	4.3	149	0.3	29.7	1.26
	P6	1.35	21.0	0.91	0.285	2.39	0.040	73.6	3.2	59.3	4.3	149	0.5	18.6	1.26
VI	P7	0.8	21.0	1.89	0.284	2.64	0.040	73.8	6.6	65.3	9.0	343	1.5	9.8	1.26
	P8	0.9	21.0	1.89	0.356	2.64	0.032	59.0	5.3	81.7	9.0	343	0.9	15.4	1.26
	P9	1.0	21.0	1.89	0.394	2.64	0.029	53.2	4.8	90.6	9.0	343	0.8	18.9	1.26
	P10	1.15	21.0	1.89	0.398	2.64	0.029	52.7	4.7	91.4	9.0	343	0.8	19.3	1.26
	P11	1.25	21.0	1.89	0.360	2.64	0.032	58.2	5.2	82.8	9.0	343	0.9	15.8	1.26
	P12	1.35	21.0	1.89	0.285	2.64	0.040	73.6	6.6	65.5	9.0	343	1.5	9.9	1.26
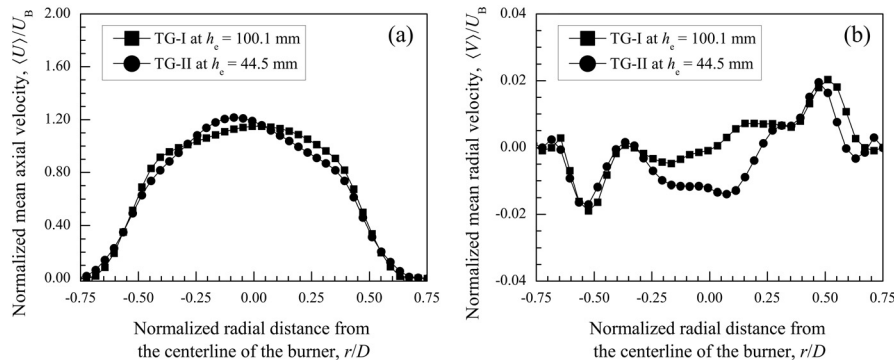
Fig. 3. Normalized mean (a) axial and (b) radial velocity profiles with respect to the normalized radial distance from the centerline of the burner at $h/D = 0.5$.

burner are shown in Fig. 4(a)–(c). It is observed that the profiles of $\langle u^2 \rangle^{1/2}$ are comparatively uniform within 30% variations for $r/D <$ 0.25, whereas the variations of $\langle v^2 \rangle^{1/2}$ and u' are approximately 10%. All of these profiles have peaks near the rim of the burner. These peaks may be attributed to the existence of shear layers. Similar

observations were previously reported in the literature, see Fig. 5 in [28], Figs. 3 and 4 in [30], Fig. 5.8(a) in [39], and Fig. 2 in [24]. Chen et al. [40] showed that the total turbulence intensity value along the axial direction on the centerline of the burner does not vary for reacting conditions. They showed that these values are similar to
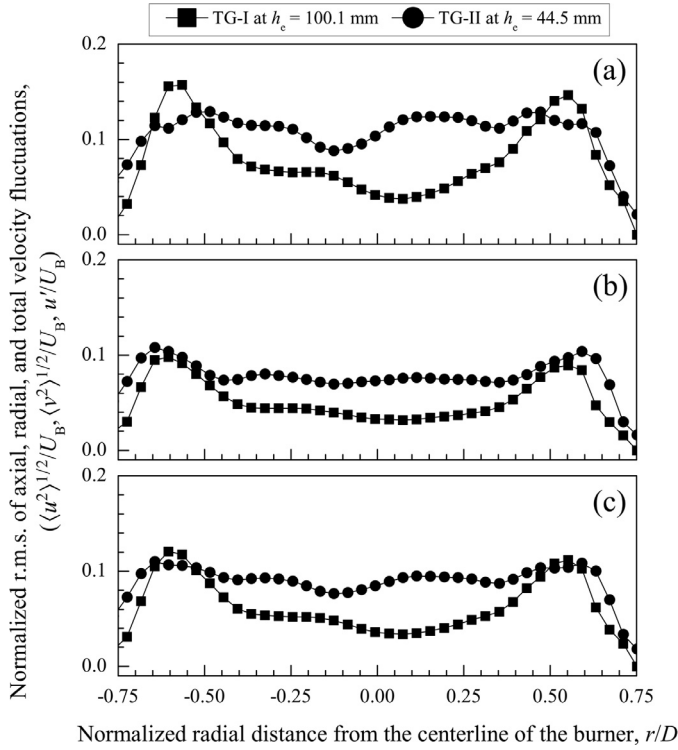
Fig. 4. Normalized r.m.s. of (a) axial, (b) radial, and (c) total velocity fluctuations with respect to the normalized radial distance from the centerline of the burner at $h/D = 0.5$.
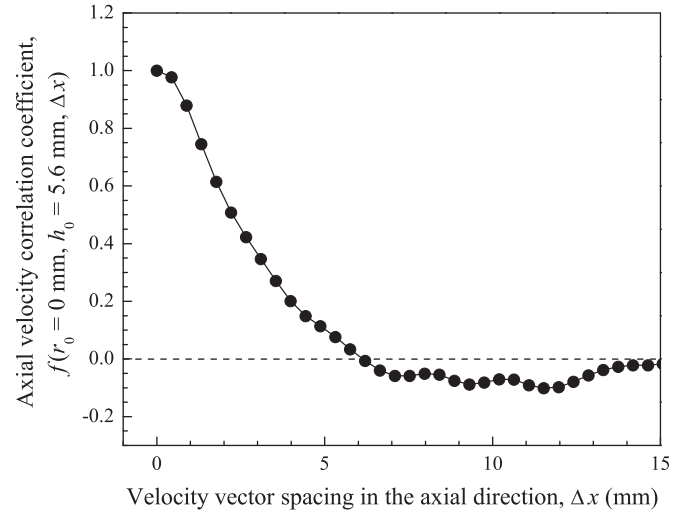

Fig. 5. Axial velocity correlation coefficient with respect to the velocity vector spacing in the axial direction at $r_0 = 0$ mm and $h_0 = 5.6$ mm. The TG-II which was mounted at $h_e = 44.5$ mm was utilized to generate the turbulence for this condition.

the total turbulence intensity value which was measured near the burner exit for non-reacting conditions. Therefore, it is reasonable to assume that the value of the total turbulence intensity which was measured near the burner exit for non-reacting conditions is an appropriate choice for characterizing this parameter for reacting conditions. Therefore, the representative value of the total turbulence intensity was estimated by taking an average over local total turbulence intensities in a region between $-0.25 < r/D < 0.25$ and $0.2 < h/D < 0.5$ for each experimental condition. The representative values of total turbulence intensity for all operating conditions are summarized in Table 2. It is shown that the total turbulence intensity increased by a factor of 2 by changing the perforated plate and its upstream position from the burner exit from TG-I at $h_e = 100.1$ mm to TG-II at $h_e = 44.5$ mm, see Table 2. Following Benedict and Gould [41], the uncertainty associated with the total turbulence intensity was calculated to be approximately 6%.

The longitudinal integral length scale at a specific location of r_0 and h_0, $\Lambda_L(r_0, h_0)$, was acquired from the axial velocity correlation coefficient, $f(r_0, h_0, \Delta x)$ [42]. This coefficient was obtained from the following formula:

$$f(r_0, h_0, \Delta x) = \frac{\langle u(r_0, h_0)u(r_0, h_0 + \Delta x)\rangle}{\langle u(r_0, h_0)^2\rangle}, \qquad (2)$$

where u is the velocity fluctuations in the axial direction, and Δx is the velocity vector spacing in the axial direction. A representative profile of the axial velocity correlation coefficient at $r_0 = 0$ mm and $h_0 = 5.6$ mm is shown in Fig. 5. Similar plots were previously presented in the literature, see Fig. 6 in [28], Fig. 7(a) in [30], Fig. 5.3 in [39], Fig. 3.21 in [26], and Fig. 3 in [24].

The longitudinal integral length scale was then estimated using the following expression:

$$\Lambda_L(r_0, h_0) = \int_0^{\Delta x_L^*} f(r_0, h_0, \Delta x) d\Delta x, \qquad (3)$$

where Δx_L^* is the first location at which the axial velocity correlation coefficient is equal to zero. The representative value of the longitudinal integral length, Λ_L, for each experimental condition was determined by taking an average over local longitudinal integral length scales in a region between $-0.25 < r/D < 0.25$ and $0.2 < h/D < 0.5$. The longitudinal integral length scale values for all experimental conditions are summarized in Table 2. The uncertainty associated with the longitudinal integral length scale was estimated to be approximately 25%. The longitudinal integral length scale values produced by both turbulence generators, that is, TG-I and TG-II, are close to each other (the difference is about 10%). This makes it possible to evaluate the influence of the total turbulence intensity on the flame brush characteristics, instantaneous flame front structures, and burning velocities of premixed turbulent flames when the longitudinal integral length scale is kept constant.

As stated earlier, the summary of all experimental conditions is tabulated in Table 2. The unstrained premixed laminar burning velocity, S_L^0, was calculated using the Cantera package [43] with the GRI-3.0 mechanism [44] for methane/– and ethane/air flames, whereas this mechanism did not provide an accurate results for propane/air flames. Therefore, experimental data of S_L^0 reported in [45] were utilized for propane/air flames. The Zel'dovich thickness, δ_f, was determined by calculating the ratio of the reactants mass diffusivity to the unstrained premixed laminar burning velocity [1]. The mass diffusivity for each hydrocarbon/air mixture tested in this study was determined using a methodology described in Reid et al. [46]. For each set of experiments, the values of the equivalence ratio were selected in a manner that there exist flame conditions on both the lean/stoichiometric and rich mixtures with identical unstrained premixed laminar burning velocities. For example, the values of S_L^0 for Flames P7 and P12 are almost similar, whereas the equivalence ratios are different. This results in having two flame conditions on both lean/stoichiometric and rich mixtures for each set of experiments with constant unstrained premixed laminar burning velocity, non-dimensional bulk flow velocity (U_B/S_L^0), non-dimensional turbulence intensity (u'/S_L^0), and non-dimensional longitudinal integral length scale (Λ_L/δ_f). This permits to isolate the effect of thermo-diffusive properties on the flame brush characteristics, instantaneous flame front structures, and burning velocities. The turbulent Reynolds, Karlovitz, and Damköhler numbers were estimated from $Re_{\Lambda_L} = u'\Lambda_L/\nu$, $Ka = (\delta_f/\eta)^2$, and $Da = \Lambda_L S_L^0/\delta_f u'$, respectively, where ν is the reactants kinematic viscosity obtained from [46], and η is the Kolmogorov length scale evaluated from $\eta = \Lambda_L Re_{\Lambda_L}^{-3/4}$ [47]. The Schmidt number, Sc, was determined by calculating the ratio of the reactants kinematic viscosity to the mass diffusivity.
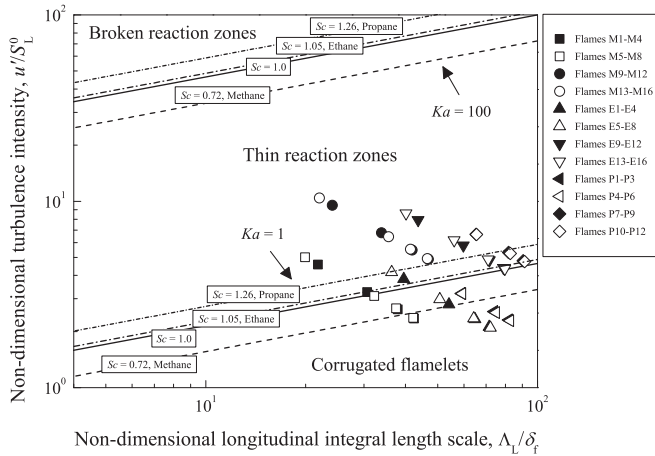
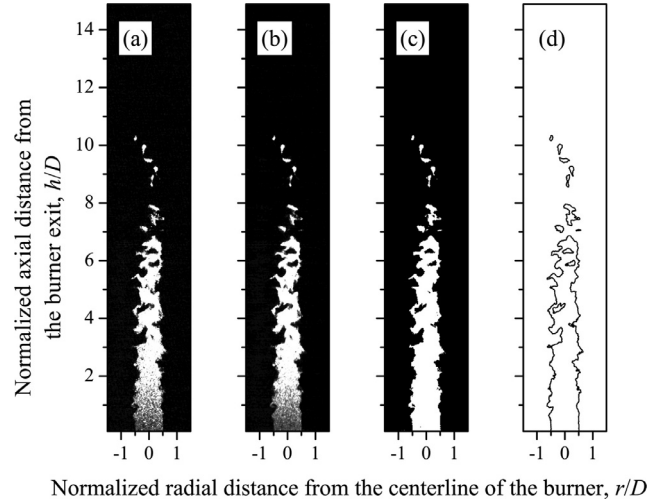Fig. 6. Experimental data on a Borghi–Peters regime diagram for premixed turbulent combustion [13,48].

Fig. 7. Image processing procedure utilized for determining the flame front locations. (a) Raw Mie scattering image, (b) filtered image, (c) binarized image, and (d) flame front locations for Flame M4.

The experimental data from the current study are superimposed on a Borghi–Peters regime diagram for premixed turbulent combustion [13,48], as shown in Fig. 6. The locations of the lines that separate the corrugated flamelets regime from the thin reaction zones regime and the latter regime from the broken reaction zones regime changed using different hydrocarbon/air mixtures. These lines were obtained using a methodology described by Tamadonfar and Gülder [24]. It is observed that all test conditions are located in the corrugated flamelets and thin reaction zones regimes.

2.3. Flame front visualization

The flame front corrugations were visualized using the Mie scattering technique. This technique has been extensively used for flame front visualization of Bunsen-type flames [2,3,27,32,49–56], V-shaped flames [2,36,37,57–59], and swirl-stabilized flames [60–62]. The laser, light sheet optical assembly, CCD camera, and bandpass filter used in this technique were similar to the equipments utilized in the particle image velocimetry technique described in detail in Section 2.2. The camera was equipped with a Nikon Micro-Nikkor 60 mm lens operating at $f/8.0$. The field-of-view imaged by the current system was approximately 187×187 mm^2 with a resolution of 91.2 μm/pixel. Five hundred images were captured at a frequency of 6 Hz using the DaVis 7.2 software for each flame condition. A raw Mie scattering image for a representative flame condition, Flame M4, is shown in Fig. 7(a). A 3×3 pixels^2 median filter was applied on each raw image in order to reduce noise, as shown in Fig. 7(b). The filtered images were then binarized by assigning a threshold value for the light intensity. For each binarized image, the pixel value of 0 (white zone) indicates the progress variable of 0, that is, unburned zone, and the pixel value of 1 (black zone) specifies the progress variable of 1, that is, fully burned zone, as shown in Fig. 7(c). The instantaneous flame front locations for each binarized image were determined using a script written in MATLAB, as shown in Fig. 7(d).

3. Results and discussion

3.1. Characteristic flame height

A contour plot of the mean progress variable, $\langle c \rangle$, was obtained by taking an average over 500 instantaneous binarized images for each flame condition, as shown in Fig. 8. The characteristic flame height, $H_{\langle c \rangle = 0.5}$, is considered as the distance from the burner exit to the half-burning surface, that is, the iso-contour of $\langle c \rangle = 0.5$, determined on the centerline of the burner, as shown in Fig. 8. The characteristic
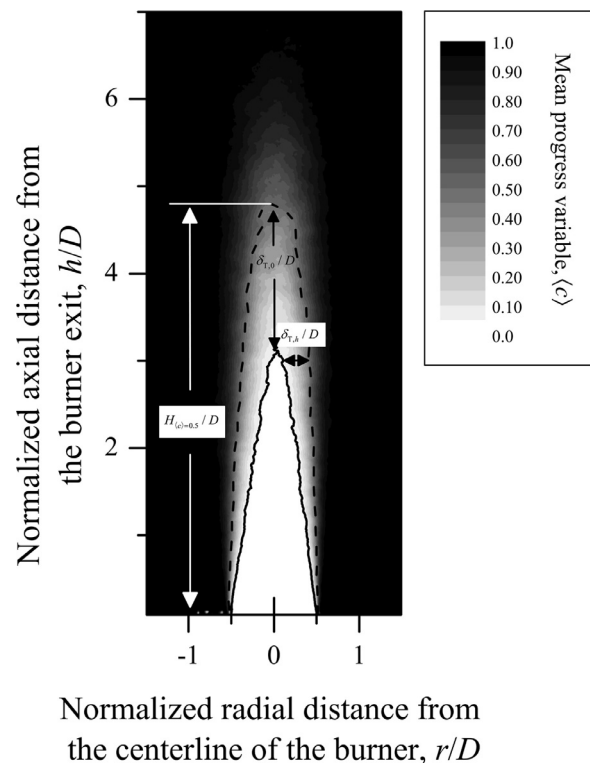
Fig. 8. Mean progress variable contour for Flame E13. Solid and dash lines indicate the iso-contours of $\langle c \rangle = 0.05$ and 0.5, respectively. The definitions of the characteristic flame height, $H_{\langle c \rangle = 0.5}$, centerline mean flame brush thickness, $\delta_{T,0}$, and horizontal mean flame brush thickness, $\delta_{T,h}$, are shown on this contour.

flame height is usually employed for testing the numerical models for premixed turbulent Bunsen flames, see, for example, the large-eddy simulation (LES) results in [63–65], and the direct numerical simulation (DNS) results in [66].

The variations of the normalized characteristic flame height, $H_{\langle c \rangle = 0.5}/D$, with respect to the equivalence ratio, ϕ, are shown in Fig. 9(a)–(c). The normalized characteristic flame height decreased significantly with increasing equivalence ratio from 0.7 to 1.0 for methane/– and ethane/air flames, and 0.8–1.0 for propane/air flames. This trend could be referred to the augmentation of global reaction rate due to an increase in flame temperature. Similar observations
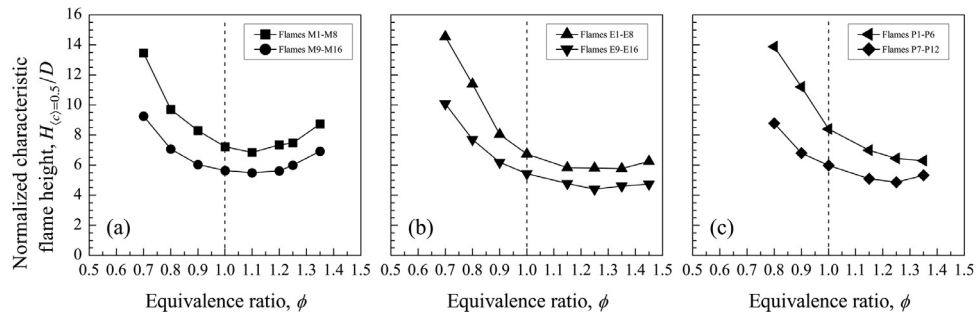
Fig. 9. Normalized characteristic flame height with respect to the equivalence ratio for (a) methane/air, (b) ethane/air, and (c) propane/air flames.

Table 3

Summary of experimental results. Symbols: ϕ = equivalence ratio; U_B = bulk flow velocity; u' = total turbulence intensity; S_L^0 = unstrained premixed laminar burning velocity; Λ_L = longitudinal integral length scale; δ_f = Zel'dovich thickness; $H_{\langle c \rangle = 0.5}$ = characteristic flame height; $\delta_{T,0}$ = centerline mean flame brush thickness; $\langle V_f \rangle$ = mean volume of the turbulent flame region; $\langle W_f \rangle$ = mean fuel consumption rate; $\Sigma_{S,2D,max}$ = maximum two-dimensional flame surface density; A_w = wrinkled flame surface area; A_u = unwrinkled flame surface area. The indexes S and G in the last three columns refer to the Shepherd's method and gradient of the progress variable method, respectively.

Set of exp.	Flame	ϕ (−)	U_B/S_L^0 (−)	u'/S_L^0 (−)	Λ_L/δ_f (−)	$H_{\langle c \rangle=0.5}$ (mm)	$\delta_{T,0}$ (mm)	$\langle V_f \rangle$ (mm³)	$\langle W_f \rangle \times 10^9$ (kg/mm³s)	$\Sigma_{S,2D,max}$ (1/mm)	$(A_w/A_u)_S$ (−)	$(A_w/A_u)_G$ (−)
I	M1	0.7	105.7	4.6	21.8	149.6	63.5	28,608	3.2	0.52	4.58	4.53
	M2	0.8	75.1	3.3	30.6	107.9	42.5	16,759	6.1	0.57	4.24	4.18
	M3	0.9	60.7	2.6	37.9	92.2	35.7	12,569	9.1	0.60	4.08	4.01
	M4	1.0	54.3	2.4	42.4	80.4	26.9	10,265	12.3	0.61	4.08	4.00
	M5	1.1	54.6	2.4	42.2	76.1	25.1	9,411	14.6	0.64	4.03	3.95
	M6	1.2	61.5	2.7	37.5	81.7	28.6	9,550	15.6	0.63	3.86	3.78
	M7	1.25	71.6	3.1	32.2	83.1	26.1	9,874	15.6	0.63	3.77	3.69
	M8	1.35	115.6	5.0	19.9	97.2	27.8	11,497	14.3	0.61	3.63	3.56
II	M9	0.7	105.7	9.5	24.1	103.0	49.1	29,697	3.1	0.47	5.81	5.79
	M10	0.8	75.1	6.8	33.8	78.6	31.0	18,567	5.5	0.51	4.74	4.74
	M11	0.9	60.7	5.5	41.9	67.1	25.4	14,030	8.2	0.53	4.51	4.50
	M12	1.0	54.3	4.9	46.8	62.7	23.6	12,057	10.5	0.54	4.30	4.29
	M13	1.1	54.6	4.9	46.6	61.0	21.8	11,447	12.0	0.55	4.18	4.16
	M14	1.2	61.5	5.5	41.4	62.5	21.8	11,520	12.9	0.54	4.10	4.08
	M15	1.25	71.6	6.4	35.5	66.7	24.8	11,852	13.0	0.53	4.02	4.00
	M16	1.35	115.6	10.4	22.0	76.9	27.5	14,407	11.4	0.49	3.90	3.87
III	E1	0.7	88.2	3.8	39.5	161.8	67.9	25,764	3.9	0.57	4.39	4.30
	E2	0.8	64.5	2.8	54.1	126.6	51.0	16,264	7.0	0.64	4.54	4.41
	E3	0.9	53.7	2.3	64.8	89.5	34.7	11,493	11.0	0.70	5.21	5.03
	E4	1.0	48.8	2.1	71.5	74.9	29.5	8,948	15.7	0.73	5.29	5.10
	E5	1.15	48.3	2.1	72.2	64.9	22.0	7,424	21.5	0.74	5.24	5.03
	E6	1.25	54.2	2.3	64.3	64.7	23.4	7,290	23.7	0.70	4.32	4.21
	E7	1.35	68.7	3.0	50.8	64.2	20.4	7,653	24.2	0.72	4.40	4.28
	E8	1.45	95.9	4.2	36.3	69.6	24.1	8,610	23.0	0.67	4.33	4.24
IV	E9	0.7	88.2	7.9	43.7	112.2	54.8	26,621	3.8	0.53	6.05	5.97
	E10	0.8	64.5	5.8	59.7	85.7	41.0	16,651	6.8	0.55	5.14	5.07
	E11	0.9	53.7	4.8	71.6	68.7	29.9	12,341	10.3	0.57	4.84	4.78
	E12	1.0	48.8	4.4	78.9	60.5	25.4	10,161	13.8	0.59	4.70	4.63
	E13	1.15	48.3	4.3	79.7	53.1	19.0	8,402	19.0	0.60	4.54	4.49
	E14	1.25	54.2	4.9	71.0	48.9	18.8	7,687	22.5	0.65	5.04	4.94
	E15	1.35	68.7	6.2	56.1	51.3	20.2	8,307	22.3	0.64	4.96	4.86
	E16	1.45	95.9	8.6	40.1	52.6	19.0	8,475	23.4	0.64	4.75	4.66
V	P1	0.8	73.8	3.2	59.1	154.3	56.8	22,756	5.4	0.55	3.52	3.48
	P2	0.9	59.0	2.6	74.0	124.5	46.2	15,857	8.6	0.57	3.57	3.53
	P3	1.0	53.2	2.3	82.0	93.5	34.0	11,318	13.3	0.60	3.79	3.72
	P4	1.15	52.7	2.3	82.8	77.8	26.6	8,672	19.8	0.66	3.71	3.65
	P5	1.25	58.2	2.5	74.9	71.6	23.3	8,346	22.3	0.66	3.89	3.82
	P6	1.35	73.6	3.2	59.3	70.0	24.1	8,046	24.8	0.67	4.00	3.93
VI	P7	0.8	73.8	6.6	65.3	97.6	49.4	24,074	5.1	0.52	6.04	6.00
	P8	0.9	59.0	5.3	81.7	75.6	35.0	14,663	9.3	0.56	5.28	5.22
	P9	1.0	53.2	4.8	90.6	66.5	29.2	11,761	12.8	0.59	5.00	4.92
	P10	1.15	52.7	4.7	91.4	56.7	24.5	8,804	19.5	0.62	4.96	4.86
	P11	1.25	58.2	5.2	82.8	54.2	22.7	8,791	21.1	0.64	4.99	4.89
	P12	1.35	73.6	6.6	65.5	59.2	21.3	8,339	23.9	0.64	4.41	4.34

were previously reported in [24,31,67,68]. The variations of $H_{\langle c \rangle = 0.5}/D$ were found to be insignificant with increasing equivalence ratio from 1.15 to 1.45 for ethane/air flames and 1.15–1.35 for propane/air flames, whereas $H_{\langle c \rangle = 0.5}/D$ increased slightly by increasing the equivalence ratio from 1.1 to 1.35 for methane/air flames. This trend could be attributed to the insignificant variations of the turbulent burning velocity for rich ethane/– and propane/air flames even though the flame temperature decreased for these flame conditions, whereas the burning velocity decreased for rich methane/air flames with increasing equivalence ratio. This issue will be discussed in detail in

Section 3.9. Results show that by a two-fold increase in the total turbulence intensity, $H_{\langle c \rangle = 0.5}/D$ decreased by approximately 20–31% for methane/– and ethane/air flames, and 15–39% for propane/air flames when the equivalence ratio, non-dimensional bulk flow velocity, and non-dimensional longitudinal integral length scale were kept constant. For example, $H_{\langle c \rangle = 0.5}/D$ for Flame M12 is 22% shorter than $H_{\langle c \rangle = 0.5}/D$ for Flame M4. This could be due to an increase in the turbulent burning velocity which will be explained in Section 3.9. A similar trend was previously reported for lean to stoichiometric methane/air flames in [24]. It is observed that the normalized characteristic flame height for lean/stoichiometric conditions is higher than the corresponding value for rich mixtures under constant unstrained premixed laminar burning velocity, non-dimensional bulk flow velocity, non-dimensional turbulence intensity, and non-dimensional longitudinal integral length scale. For example, $H_{\langle c \rangle = 0.5}/D$ for Flame E2 is two-times higher than $H_{\langle c \rangle = 0.5}/D$ for Flame E7. This difference could be due to the different thermo-diffusive characteristics of lean/stoichiometric and rich mixtures. The characteristic flame height values for all operating conditions are summarized in Table 3.

Further investigation showed that the product of normalized characteristic flame height and turbulent Karlovitz number has a power-law relation with the turbulent Damköhler number using the following expression:

$$(H_{\langle c \rangle = 0.5}/D)Ka = \gamma_1 Da^{\gamma_2}, \tag{4}$$

where γ_1 and γ_2 are the coefficient and power constants. The product of normalized characteristic flame height and turbulent Karlovitz number with respect to the turbulent Damköhler number for lean/stoichiometric methane/–, ethane/–, and propane/air flames is shown in Fig. 10(a), and for rich methane/–, ethane/–, and propane/air flames is shown in Fig. 10(b). It is observed that the value of γ_1 varies between lean/stoichiometric and rich mixtures, whereas the value of γ_2 does not change significantly. The above formulation suggests that the characteristic flame height can be estimated by knowing the turbulent Karlovitz and Damköhler numbers.

3.2. Mean flame brush thickness

The mean flame brush thickness, δ_T, is the region in space where the reaction layers are positioned [7]. It is essential to investigate the behavior of the mean flame brush thickness experimentally. This investigation helps to assess the accuracy of numerical models [7,22]. Lipatnikov and Chomiak [22] believed that the mean flame brush thickness is a significant combustion characteristic, and it should not be utilized exclusively for ranking numerical models. In this study, the mean flame brush thickness is divided into two parts: (1) the centerline mean flame brush thickness, $\delta_{T, 0}$, and (2) the horizontal mean flame brush thickness, $\delta_{T, h}$. The locations of these thicknesses on the mean progress variable contour are demonstrated in Fig. 8.

There exist different definitions in the literature for the evaluation of the mean flame brush thickness. For example, Namazian et al. [69] and Kheirkhah and Gülder [36,37] determined the mean flame brush thickness using the maximum gradient method, whereas Gouldin and Miles [70], Lee et al. [71], Griebel et al. [31], Venkateswaran [72], and Tamadonfar and Gülder [24] evaluated the mean flame brush thickness by finding the distance between two specific mean progress variable surfaces. It should be stated that using different definitions for the estimation of the mean flame brush thickness result in different quantitative values, whereas the qualitative trends remain unaltered, as shown in Fig. 11. Experimental results of Venkateswaran [72] displayed a similar observation. In this study, the mean flame brush thickness was determined by finding the distance between the leading edge of the flame, that is, the iso-contour of $\langle c \rangle = 0.05$, and the half-burning surface, that is, the iso-contour of $\langle c \rangle = 0.5$.
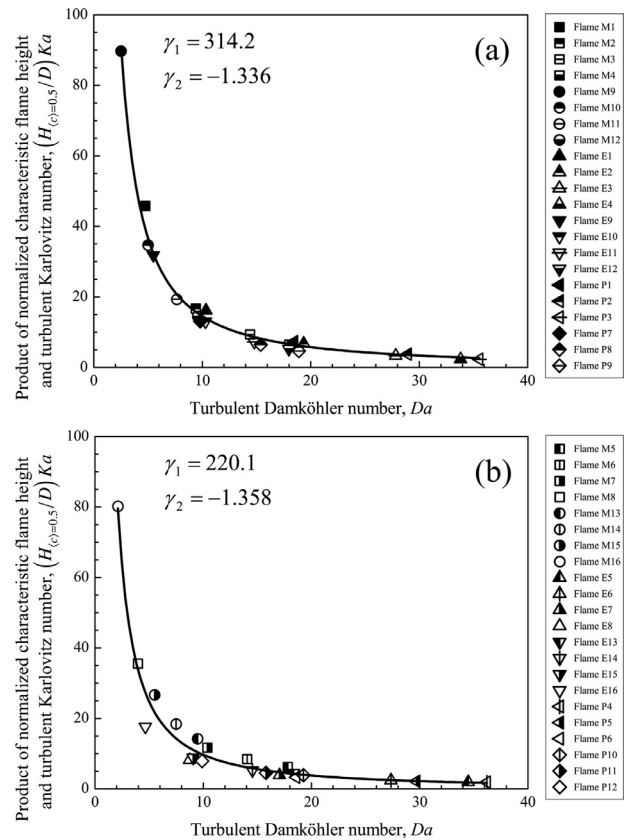

Fig. 10. Product of normalized characteristic flame height and turbulent Karlovitz number with respect to the turbulent Damköhler number for (a) lean/stoichiometric methane/–, ethane/–, and propane/air flames and (b) rich methane/–, ethane/–, and propane/air flames. The solid line in each subfigure refers to the least-squares fit to the measured data.
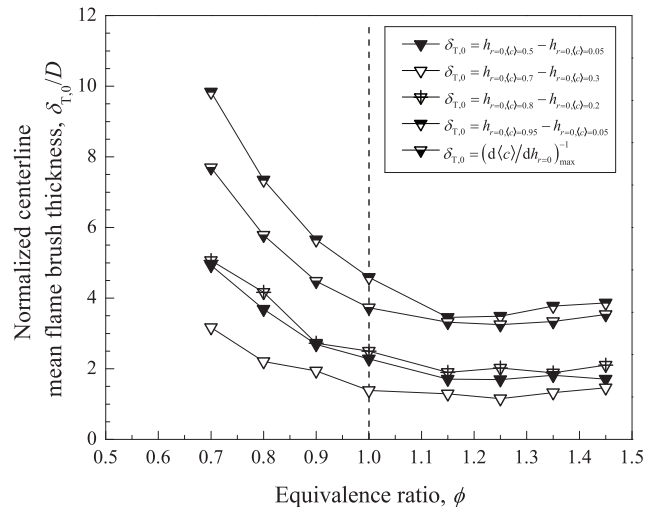

Fig. 11. Centerline mean flame brush thickness evaluated with different definitions normalized by the burner nozzle inner diameter with respect to the equivalence ratio for Flames E9–E16.

3.2.1. Centerline mean flame brush thickness

The variations of the normalized centerline mean flame brush thickness, $\delta_{T, 0}/D$, with respect to the equivalence ratio for all experimental conditions are shown in Fig. 12(a)–(c). Results show that $\delta_{T, 0}/D$ decreased significantly with increasing equivalence ratio from 0.7 to 1.0 for methane/– and ethane/air flames, and 0.8–1.0 for propane/air flames, whereas it remained relatively unchanged
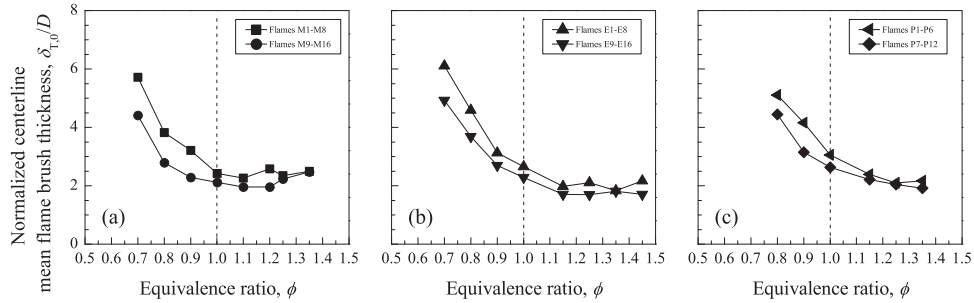
Fig. 12. Normalized centerline mean flame brush thickness with respect to the equivalence ratio for (a) methane/air, (b) ethane/air, and (c) propane/air flames.

with increasing equivalence ratio from 1.1 to 1.35 for methane/air, 1.15–1.45 for ethane/air, and 1.15–1.35 for propane/air flames. Experimental results of Griebel et al. [31] and Tamadonfar and Gülder [24] showed a similar decreasing trend for premixed turbulent methane/air flames. Results show that $\delta_{T,0}/D$ decreased by increasing the total turbulence intensity from 0.91 to 1.89 m/s when the equivalence ratio, non-dimensional bulk flow velocity, and non-dimensional longitudinal integral length scale were kept constant. For example, $\delta_{T,0}/D$ is equal to 5.1 for Flame P1, and it decreases to 4.4 for Flame P7 by a two-fold increase in the total turbulence intensity. This observation is in agreement with previous measurements of Tamadonfar and Gülder [24] for premixed turbulent methane/air flames. Furthermore, $\delta_{T,0}/D$ for lean/stoichiometric mixtures is observed to be higher than the corresponding value for rich mixtures with identical unstrained premixed laminar burning velocity, non-dimensional bulk flow velocity, non-dimensional turbulence intensity, and non-dimensional longitudinal integral length scale. The centerline mean flame brush thickness values for all operating conditions are tabulated in Table 3.

The product of normalized centerline mean flame brush thickness and turbulent Karlovitz number has a power-law relation with the turbulent Damköhler number using the following expression:

$$(\delta_{T,0}/D)Ka = \gamma_3 Da^{\gamma_4}, \tag{5}$$

where γ_3 and γ_4 are the coefficient and power constants. The product of normalized centerline mean flame brush thickness with respect to the turbulent Damköhler number for lean/stoichiometric test conditions is shown in Fig. 13(a), and for rich test conditions is shown in Fig. 13(b). The value of γ_3 changed between lean/stoichiometric and rich mixtures, whereas the value of γ_4 stayed relatively constant.

The mean progress variable profiles on the centerline of the burner mimicked the behavior of a complementary error function, Fig. 14(a)–(d). Experimental measurements of Halter et al. [73] showed a similar observation. Results show that these profiles collapsed to a universal curve for all experimental conditions when the centerline distance across the flame brush, ζ_0, was normalized by the centerline mean flame brush thickness, $\delta_{T,0}$. The centerline distance across the flame brush was determined using the following expression:

$$\zeta_0 = h_{r=0} - h_{r=0, \langle c \rangle = 0.5}. \tag{6}$$

It is observed that these profiles are not sensitive to the equivalence ratio (for example, Flames M9–M16), total turbulence intensity (for example, Flames E1 and E9), different thermo-diffusive characteristics (for example, Flames P1 and P6), and the fuel type (Fig. 14(d)).

3.2.2. Horizontal mean flame brush thickness

The variations of the normalized horizontal mean flame brush thickness, $\delta_{T,h}/D$, with respect to the normalized axial distance from the burner exit, h/D, are shown in Fig. 15 for methane/air, Fig. 16 for ethane/air, and Fig. 17 for propane/air flames. It is observed that $\delta_{T,h}/D$ increases with increasing h/D for each flame condition. This

observation is usually described in the literature by the Taylor theory of turbulent diffusion [22]. Similar observations were previously reported, see, for example, [3,24,37,67,69,72]. Results show that for methane/air flames, $\delta_{T,h}/D$ was independent of the equivalence ratio for $h/D < 2$. This indicates that the flame front wrinkling is restricted due to the existence of anchoring boundary condition near the burner exit [72]. However, at larger h/D, the normalized horizontal mean flame brush thickness increased with increasing equivalence ratio from 0.7 to 1.0 (Fig. 15(a) and (c)), whereas it decreased with increasing equivalence ratio from 1.1 to 1.35 (Fig. 15(b) and (d)). This observation suggests that increasing the unstrained premixed
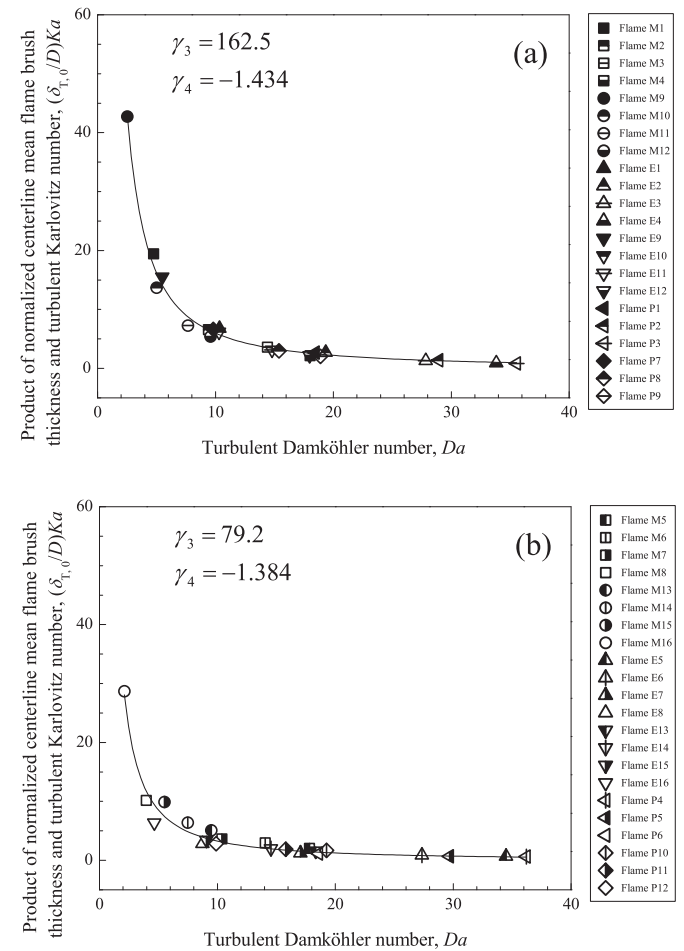

Fig. 13. Product of normalized centerline mean flame brush thickness and turbulent Karlovitz number with respect to the turbulent Damköhler number for (a) lean/stoichiometric methane/–, ethane/–, and propane/air flames and (b) rich methane/–, ethane/–, and propane/air flames. The solid line in each subfigure refers to the least-squares fit to the measured data.
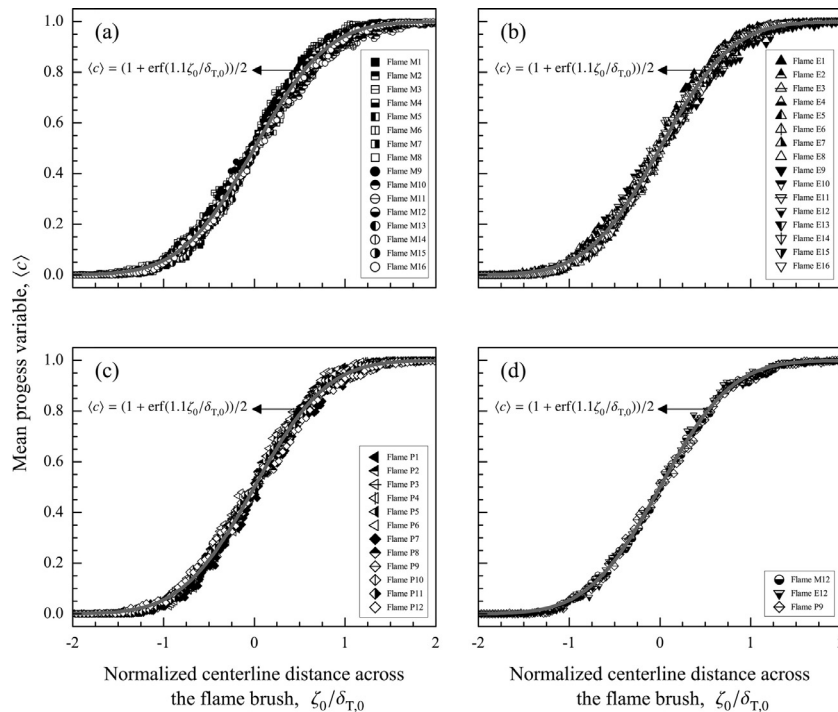
Fig. 14. Mean progress variable profiles on the centerline of the burner with respect to the normalized centerline distance across the flame brush for (a) methane/air, (b) ethane/air, (c) propane/air flames, and (d) three representative flame conditions.
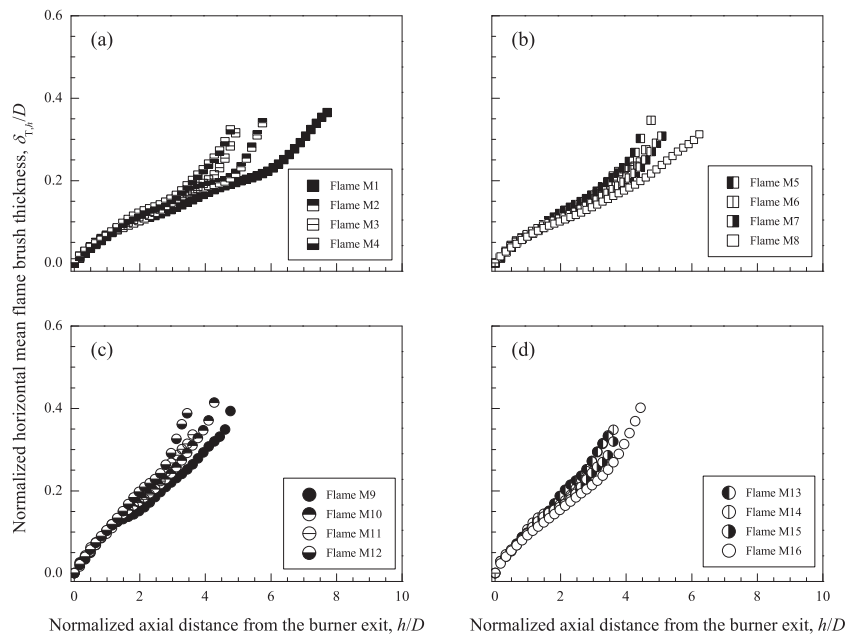

Fig. 15. Normalized horizontal mean flame brush thickness with respect to the normalized axial distance from the burner exit for (a) Flames M1–M4, (b) Flames M5–M8, (c) Flames M9–M12, and (d) Flames M13–M16.

laminar burning velocity for methane/air flames (increasing equivalence ratio from 0.7 to 1.0, and decreasing equivalence ratio from 1.35 to 1.1) results in enlarging the zone occupied by the wrinkled flamelets. Similar observations were previously reported in [24] for lean to stoichiometric methane/air Bunsen flames and in [69] for lean methane/– and ethylene/air V-shaped flames. In addition, $\delta_{T,h}/D$ increased by increasing the total turbulence intensity from 0.91 to 1.89 m/s under constant equivalence ratio, non-dimensional bulk flow velocity, and non-dimensional longitudinal integral length scale, see,

for example, Flames M3 and M11. This trend implies that increasing the total turbulence intensity results in an increase in the flame front wrinkling which enlarges the region occupied by the wrinkled flamelets. Similar trends were previously observed in the literature, see Fig. 107 in [72] for lean syngas/air Bunsen flames, and Fig. 11 in [24] for lean to stoichiometric methane/air Bunsen flames. The normalized horizontal mean flame brush thicknesses at different normalized axial distances from the burner exit were approximately equal for lean/stoichiometric and rich methane/air flames when
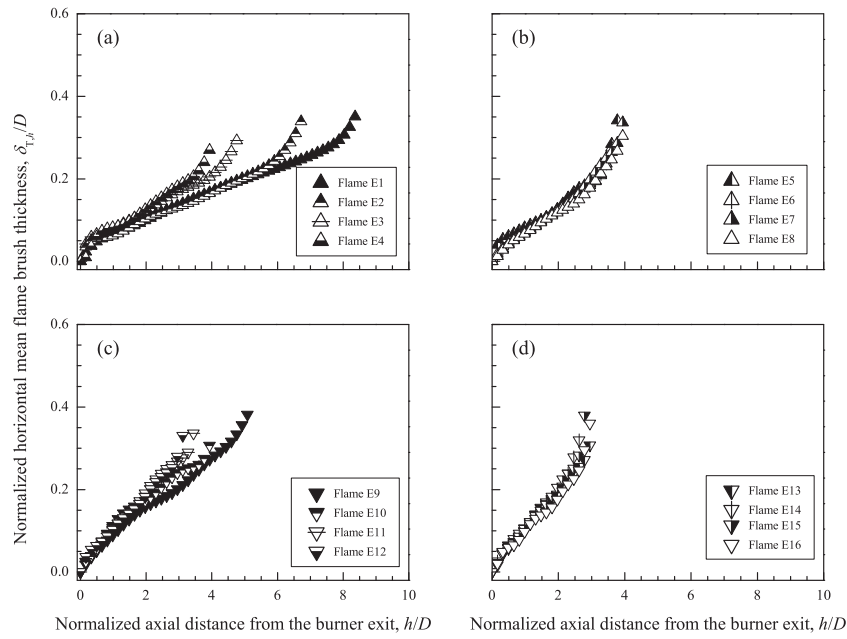
Fig. 16. Normalized horizontal mean flame brush thickness with respect to the normalized axial distance from the burner exit for (a) Flames E1–E4, (b) Flames E5–E8, (c) Flames E9–E12, and (d) Flames E13–E16.
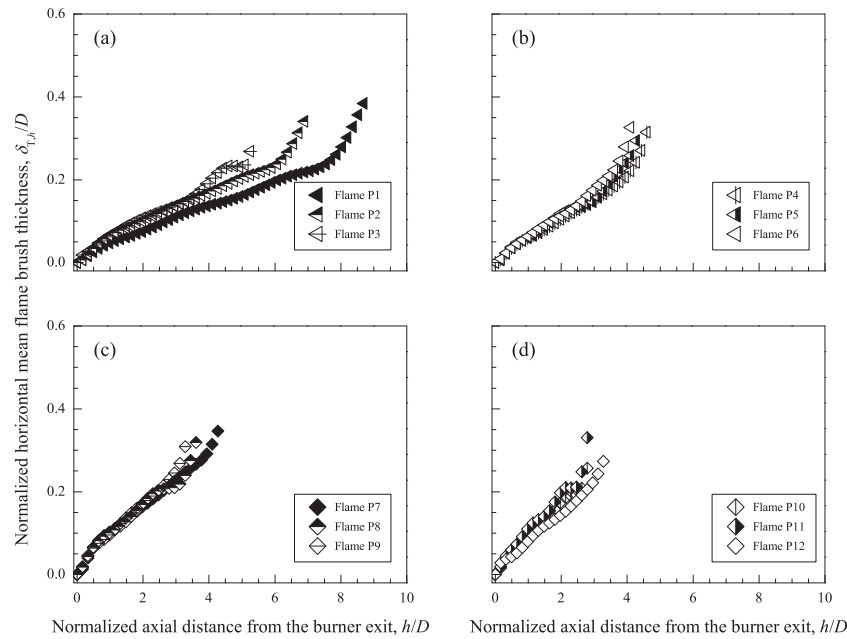

Fig. 17. Normalized horizontal mean flame brush thickness with respect to the normalized axial distance from the burner exit for (a) Flames P1–P3, (b) Flames P4–P6, (c) Flames P7–P9, and (d) Flames P10–P12.

the unstrained premixed laminar burning velocity, non-dimensional bulk flow velocity, non-dimensional turbulence intensity, and non-dimensional longitudinal integral length scale were kept constant, see, for example, Flames M9 and M16. This trend shows that the horizontal mean flame brush thickness is not sensitive to the different thermo-diffusive characteristics of methane/air flames.

The normalized horizontal mean flame brush thickness was independent of the equivalence ratio near the burner exit for ethane/air flames, similar to methane/air flames. By increasing the normalized axial distance from the burner exit, $\delta_{T,h}/D$ increased with increasing equivalence ratio from 0.7 to 1.0 (Fig. 16(a) and (c)). Results show that $\delta_{T,h}/D$ remained relatively constant with increasing equivalence ratio from 1.15 to 1.45 (Fig. 16(b) and (d)). The observed trend suggests

that for lean to stoichiometric ethane/air flames, increasing the unstrained premixed laminar burning velocity enlarges the wrinkled flamelets region, whereas it remains unaltered for rich ethane/air flames. Increasing the total turbulence intensity results in enlarging the horizontal mean flame brush thickness, see, for example, Flames E1 and E9. Results show that $\delta_{T,h}/D$ for very rich ethane/air flames, that is, $\phi = 1.35$ and 1.45, was larger than the corresponding value for very lean mixtures, that is, $\phi = 0.7$ and 0.8, at an identical h/D under constant unstrained premixed laminar burning velocity, non-dimensional bulk flow velocity, non-dimensional turbulence intensity, and non-dimensional longitudinal integral length scale, whereas it remained unaltered for near stoichiometric conditions, see, for example, flames with $\phi = 0.9$ and 1.25 and/or $\phi = 1.0$ and 1.15.

P. Tamadonfar, Ö.L. Gülder / Combustion and Flame 162 (2015) 4417–4441
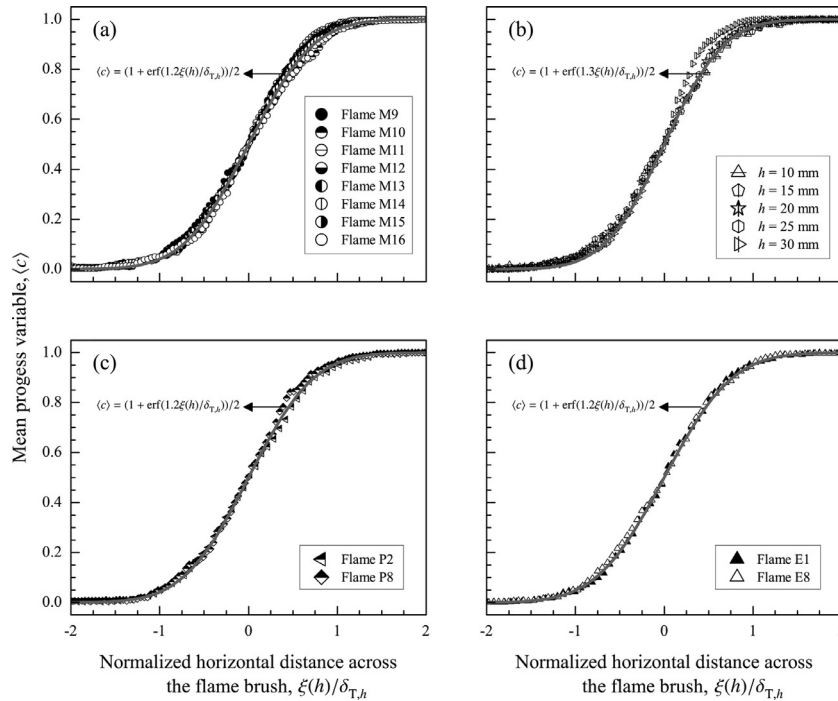

Fig. 18. Mean progress variable profiles normal to the centerline of the burner with respect to the normalized horizontal distance across the flame brush for (a) Flames M9–M16 at $h = 30$ mm, (b) Flame E3 at different axial distances from the burner exit, (c) Flames P2 and P8 at $h = 30$ mm, and (d) Flames E1 and E8 at $h = 30$ mm.

For propane/air flames, the variations of $\delta_{T,h}/D$ with respect to h/D were nearly similar to the behavior of ethane/air flames except that there exists one discrepancy. This difference occurs for the sixth set of experiments. In this set, the normalized horizontal mean flame brush thicknesses at different normalized axial distances from the burner exit were identical when S_L^0, U_B/S_L^0, u'/S_L^0, and Λ_L/δ_f were kept constant, see, for example, Flames P8 and P11.

The mean progress variable profiles normal to the centerline of the burner are well approximated by the complementary error function, as shown in Fig. 18(a)–(d). These profiles collapsed to a universal curve when the spatial coordinate normalized properly. In order to normalize the spatial coordinate, the horizontal distance across the flame brush, $\xi(h)$, was normalized by the local horizontal mean flame brush thickness. The horizontal distance across the flame brush was evaluated using the following expression:

$$\xi(h) = r(h) - r(h)_{\langle c \rangle = 0.5},\tag{7}$$

where $r(h)$ is the radial distance from the centerline of the burner at a specific axial distance from the burner exit. It is observed that the influences of the equivalence ratio (Fig. 18(a)), different axial distances from the burner exit (Fig. 18(b)), total turbulence intensity (Fig. 18(c)), and different thermo-diffusive characteristics (Fig. 18(d)) on the mean progress variable profiles are insignificant when the spatial coordinate was normalized using the above methodology. Similar observations were previously reported by Lipatnikov and Chomiak [22,23] and Tamadonfar and Gülder [24].

3.3. Mean volume of the turbulent flame region

The mean volume of the turbulent flame region, $\langle V_f \rangle$, is quantified in this section for all operating conditions. It is a region where the averaged heat release rate occurs [74,75]. In order to evaluate $\langle V_f \rangle$, the iso-contour of $\langle c \rangle = 0.05$ was selected. This iso-contour was then divided into two parts at the centerline of the burner. Each iso-contour was rotated around the centerline of the burner, and the volume was then estimated by integrating the obtained region. The representative

value of the volume for this iso-contour was evaluated by taking an average of these two magnitudes. The same method was conducted for the iso-contour of $\langle c \rangle = 0.95$. The mean volume of the turbulent flame region was obtained by subtracting the volume for $\langle c \rangle = 0.05$ from the corresponding value for $\langle c \rangle = 0.95$. Kobayashi et al. [74] and Zhang et al. [75,76] performed a similar method for evaluating $\langle V_f \rangle$ using the iso-contours of $\langle c \rangle = 0.1$ and 0.9 in their analysis. The mean volume of the turbulent flame region values for all experimental conditions are tabulated in Table 3.

The variations of the mean volume of the turbulent flame region with respect to the equivalence ratio for all operating conditions are shown in Fig. 19(a)–(c). Results show that $\langle V_f \rangle$ decreased considerably with increasing equivalence ratio from 0.7 to 1.0 for methane/– and ethane/air flames, and 0.8–1.0 for propane/air flames. Increasing the equivalence ratio from lean to stoichiometric mixtures results in a decrease in the characteristic flame height (see Fig. 9), and an increase in the horizontal mean flame brush thickness (see Figs. 15–17). Results indicate that a decrease in the flame height decreases $\langle V_f \rangle$ more than an increase in $\langle V_f \rangle$ due to the horizontal mean flame brush thickness enlargement with increasing equivalence ratio from lean to stoichiometric mixtures. The variations of $\langle V_f \rangle$ were insignificant with increasing equivalence ratio from 1.15 to 1.45 for ethane/air flames and 1.15–1.35 for propane/air flames, whereas $\langle V_f \rangle$ increased slightly with increasing equivalence ratio from 1.1 to 1.35 for methane/air flames. For ethane/– and propane/air flames, these trends were expected to be observed because both the characteristic flame height and horizontal mean flame brush thickness remained relatively unchanged for their rich mixtures. For methane/air flames, the variations of $\langle V_f \rangle$ were controlled by the alteration in the characteristic flame height, and the horizontal mean flame brush thickness reduction does not decrease $\langle V_f \rangle$ with increasing equivalence ratio from 1.1 to 1.35. Increasing the total turbulence intensity results in an increase of $\langle V_f \rangle$ under constant equivalence ratio, non-dimensional bulk flow velocity, and non-dimensional longitudinal integral length scale. For example, the mean volume of the turbulent flame region for Flame M4 is equal to 10,265 mm^3, and it increases to 12,057 mm^3
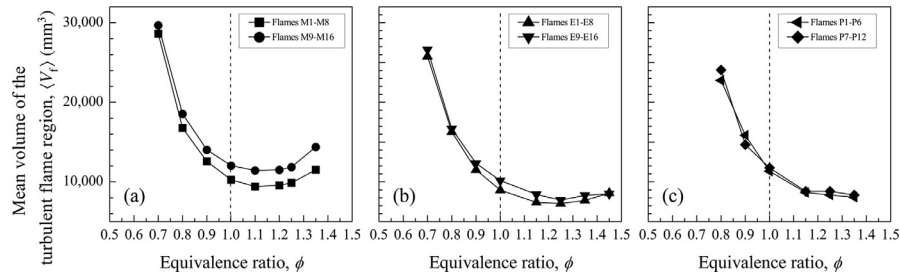
Fig. 19. Mean volume of the turbulent flame region with respect to the equivalence ratio for (a) methane/air, (b) ethane/air, and (c) propane/air flames.

for Flame M12 by increasing the total turbulence intensity from 0.91 to 1.89 m/s. This observation indicates that increasing the horizontal mean flame brush thickness due to the total turbulence intensity enhancement results in an increase of $\langle V_f \rangle$, whereas the characteristic flame height reduction due to an increase of the total turbulence intensity does not decrease $\langle V_f \rangle$. It is observed that $\langle V_f \rangle$ for rich mixtures is smaller than the corresponding value for lean/stoichiometric mixtures when the unstrained premixed laminar burning velocity, non-dimensional bulk flow velocity, non-dimensional turbulence intensity, and non-dimensional longitudinal integral length scale were fixed, see, for example, Flames E11 and E14 in Table 3. This difference may be attributed to the different thermo-diffusive characteristics of lean/stoichiometric and rich mixtures for premixed turbulent hydrocarbon/air flames.

3.4. Mean fuel consumption rate

The mean fuel consumption rate, $\langle W_f \rangle$, is proportional to the averaged heat release rate of premixed turbulent flames [74,75]. The mean fuel consumption rate was estimated using the following expression:

$$\langle W_f \rangle = \frac{\rho_r Y_f U_B A_0}{\langle V_f \rangle}, \qquad (8)$$

where ρ_r is the density of the reactants, Y_f is the mass fraction of the fuel, and A_0 is the cross-sectional area of the burner exit. The variations of the mean fuel consumption rate with respect to the equivalence ratio are shown in Fig. 20(a)–(c). The mean fuel consumption rate increased significantly with increasing equivalence ratio from 0.7 to 1.0 for methane/– and ethane/air flames, and 0.8–1.0 for propane/air flames. This observation is due to an increase in Y_f and a decrease in $\langle V_f \rangle$ with increasing equivalence ratio from lean to stoichiometric mixtures. For rich methane/– and ethane/air flames, the magnitudes of $\langle W_f \rangle$ are relatively uniform within 13–27% variations with increasing equivalence ratio under constant bulk flow velocity, total turbulence intensity, and longitudinal integral length scale. Despite the observed trend for rich methane/– and ethane/air flames, the mean fuel consumption rate increased significantly with increasing equivalence ratio from 1.15 to 1.35 for propane/air flames. The observed trend for rich mixtures may be due to an increase in the mass

fraction of the fuel with increasing equivalence ratio, whereas the insignificant variations of the mean volume of the turbulent flame region for rich ethane/– and propane/air flames and a slight increase of this parameter for rich methane/air flames seem to have a minimal effect on the mean fuel consumption rate. Results show that $\langle W_f \rangle$ decreased by increasing the total turbulence intensity under constant ϕ, U_B/S_L^0, and Λ_L/δ_f. For example, the mean fuel consumption rate is equal to 14.3×10^{-9} kg/mm^{3}s for Flame M8, and it decreases to 11.4×10^{-9} kg/mm^{3}s for Flame M16. This trend is attributed to an increase in $\langle V_f \rangle$ with increasing total turbulence intensity when the mass fraction of the fuel, non-dimensional bulk flow velocity, and non-dimensional longitudinal integral length scale were kept constant. Results show that $\langle W_f \rangle$ for rich mixtures was larger than the corresponding value for lean/stoichiometric mixtures under constant S_L^0, U_B/S_L^0, u'/S_L^0, and Λ_L/δ_f, see, for example, Flames P3 and P4. This trend may be attributed to an increase in Y_f and a decrease in $\langle V_f \rangle$ by changing the flame condition from lean/stoichiometric to rich mixtures. The mean fuel consumption rate values for all operating conditions are tabulated in Table 3.

3.5. Two-dimensional local flame front curvature

The flame front curvature, κ, discloses the effect of turbulent flow field on the flame shape and highlights the influence of the flame shape on flamelet burning [77]. Theoretical predictions indicate that the flame front curvature has a strong effect on flame propagation for flames within the thin reaction zones regime [13], whereas its influence is weak for flames within the corrugated flamelets [1]. For these reasons, it is important to reveal the behavior of the local flame front curvature of premixed turbulent flames under various conditions. To evaluate the local flame front curvature, the instantaneous flame front was filtered using a zero-phase digital filter which is a built-in script in MATLAB. This type of filter was previously utilized in the literature for the same purpose, see, for example, [33–35,78]. The length of the filter was selected to be five points, which provided a filter order of four. As a representative plot, the filtered data of an instantaneous flame front were overlaid on the raw data, as shown in Fig. 21(a). The local flame front curvature for each pixel was then
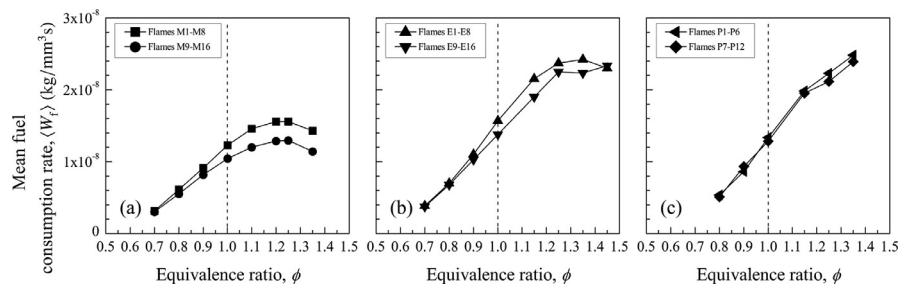

Fig. 20. Mean fuel consumption rate with respect to the equivalence ratio for (a) methane/air, (b) ethane/air, and (c) propane/air flames.
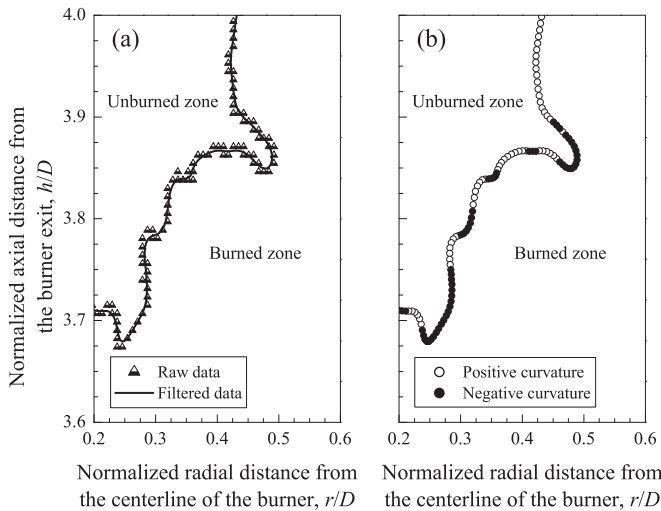
Fig. 21. (a) Instantaneous flame front for Flame E4. Triangles—raw data; solid line—filtered data. (b) The positive and negative curvature regions for the filtered instantaneous flame front for Flame E4.

evaluated using the following expression [79]:

$$\kappa(r, h) = \frac{\frac{dr}{ds}\frac{d^2h}{ds^2} - \frac{dh}{ds}\frac{dr^2}{ds^2}}{\left[\left(\frac{dr}{ds}\right)^2 + \left(\frac{dh}{ds}\right)^2\right]^{\frac{3}{2}}}, \quad (9)$$

where s is the parametrized arc length. The flame front curvature is defined to be positive (negative) when the flame front is convex (concave) toward the unburned zone, as shown in Fig. 21(b). The minimum radius of flame front that can be resolved was equal to the laser sheet thickness of approximately 300 μm. Therefore, the bounds of the resolvable flame front curvature were limited to ±3.3 mm⁻¹.

The probability density functions of the flame front curvature for all experimental conditions are shown in Fig. 22(a)–(f). These distributions are observed to be Gaussian, and they are symmetrical about zero flame front curvature. Similar observations were previously reported in the literature for premixed turbulent Bunsen flames, see, for example, [34,53–55,73,80,81], premixed turbulent low-swirl stabilized flames, see, for example, [62,82,83], partially premixed turbulent low-swirl stabilized flames, see, for example, [84], pre-

mixed turbulent propagating flame kernels, see, for example, [77,85], premixed turbulent V-shaped flames, see, for example, [36], and premixed turbulent opposed streams, see, for example, [86]. It is observed that the standard deviation of the distributions does not change with increasing equivalence ratio, see, for example, Flames E1–E8. Experimental measurements of Yuen and Gülder [87] displayed a similar trend. Results show that increasing the total turbulence intensity did not change the standard deviation of the distributions under constant equivalence ratio, non-dimensional bulk flow velocity, and non-dimensional longitudinal integral length scale, see, for example, Flames M1 and M9. This observation indicates that the flame front curvature distributions are dominant by the large-scale structures and the effect of Kolmogorov-scale eddies are minimal. This observation is in agreement with previous measurements of Yuen and Gülder [87], whereas Kostiuk et al. [86], Haq et al. [77], Gashi et al. [85], and Bayley et al. [84] observed that the flame front curvature distribution becomes wider by increasing the turbulence intensity. It is observed that the flame front curvature distributions for lean/stoichiometric and rich mixtures are identical when the unstrained premixed laminar burning velocity, non-dimensional bulk flow velocity, non-dimensional turbulence intensity, and non-dimensional longitudinal integral length scale were kept constant, see, for example, Flames M9 and M16. This observation indicates that different thermo-diffusive characteristics do not have any effect on the flame front curvature distributions. The flame front curvature results in the current study are limited to two-dimensional measurements. In addition, the flame front curvature normal to the measurement plane is not identified, and the measured curvature will be scarcely the case of the principle flame front curvature [84]. Gashi et al. [85] compared the two- and three-dimensional probability density functions of the flame front curvature for premixed turbulent propagating flame kernels using direct numerical simulation. They reported that the width of the three-dimensional flame front curvature distribution is wider than the corresponding value of the two-dimensional flame front curvature distribution. Chen et al. [88] showed that the two- and three-dimensional flame front curvature distributions for premixed turbulent stagnation-point flames are similar. On the other hand, Kerl et al. [89] reported that the probability density function of the two-dimensional flame front curvature is broader than the three-dimensional distribution for the flame stabilized on a diffuser burner. As discussed, there is no consensus regarding the effect of three-dimensionality on the flame front curvature. However, the
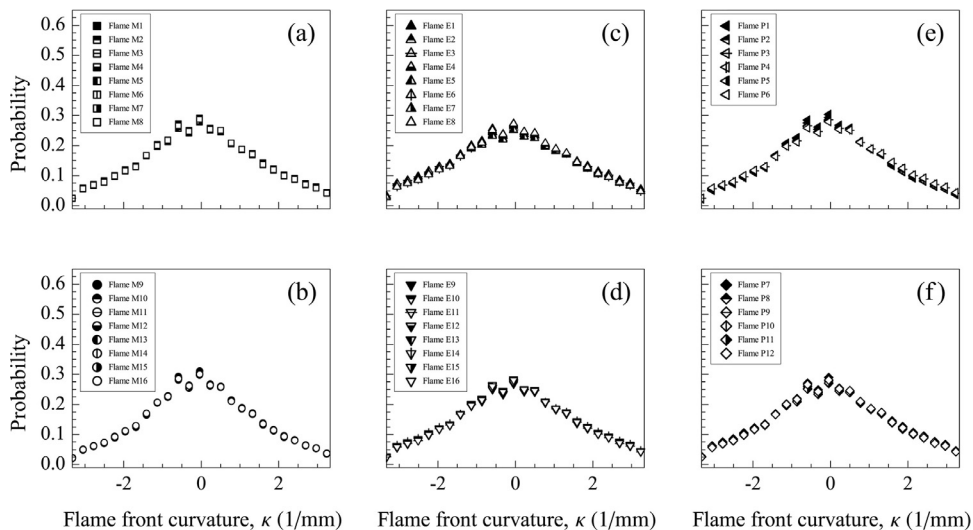

Fig. 22. Probability density functions of the flame front curvature for (a) Flames M1–M8, (b) Flames M9–M16, (c) Flames E1–E8, (d) Flames E9–E16, (e) Flames P1–P6, and (f) Flames P7–P12.
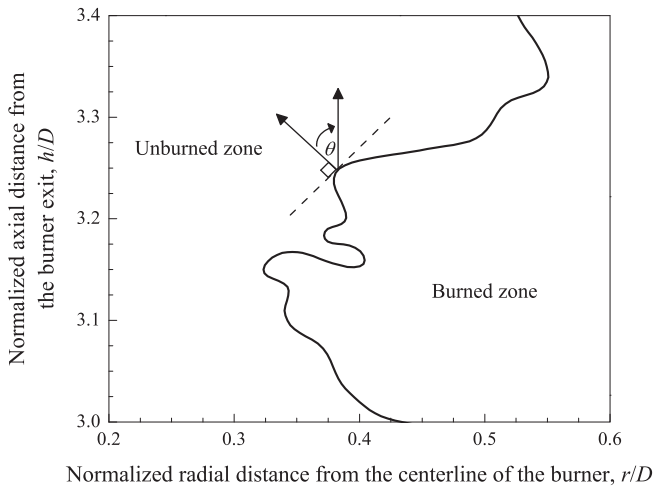
Fig. 23. Definition of the local flame front angle. The dash line is tangent to the instantaneous flame front.

Fig. 25. (a) Instantaneous flame front length as a function of the mean progress variable for Flame M4. The solid line in (a) was obtained by taking an average over 500 instantaneous flame front lengths. (b) Flame zone area as a function of the mean progress variable for Flame M4.

information obtained from the two-dimensional flame front curvature is still beneficial to understand the behavior of flame front structures.

3.6. Local flame front angle

The local flame front angle, θ, is an essential property in premixed turbulent combustion modeling. In this study, θ is evaluated by measuring the angle between the normal vector to the flame front toward the unburned zone and the axial axis, as shown in Fig. 23. A similar definition was previously utilized by Wang et al. [90] for premixed turbulent Bunsen flames. The local flame front angle was defined to be positive (negative), that is, $0° < \theta < 180°$ $(-180° < \theta < 0°)$, when it is in the counter-clockwise (clockwise) direction.

The probability density functions of the local flame front angle for all flame conditions are shown in Fig. 24(a)–(f). Results show that the shape of these profiles was bimodal with their peak values located at $\pm 90°$. This indicates that the probability of flames which propagate normal to the axial axis is more frequent. On the other hand, Wang et al. [90] showed that the peak value of the local flame front angle is occurred at 120°. They showed that this value does not change by varying the fuel type. It should be stated that the effects of the equivalence ratio, total turbulence intensity, different
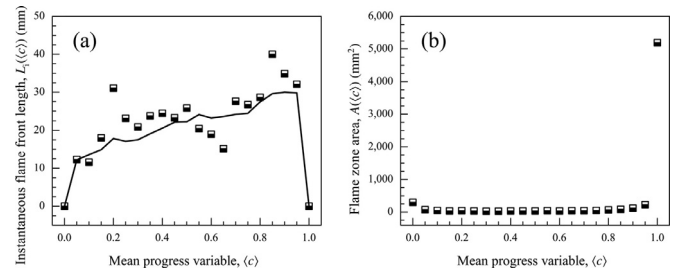
thermo-diffusive characteristics, and the fuel type are observed to be insignificant on the probability density functions of the local flame front angle in the current study.

3.7. Two-dimensional flame surface density

The flame surface density, Σ, determines how much the flame surface area is increased by wrinkling the laminar flamelets in the turbulent flow field. It is estimated by calculating the flame surface area per unit volume [91]. Two different methods for estimating the flame surface density were utilized in this study. The first method was proposed by Shepherd [59], and the second method was formulated by Pope [92]. The former method was utilized to characterize the flame surface density with respect to the mean progress variable as well as the space coordinates, whereas the latter method was only used to evaluate the flame surface density in the space coordinates.

The flame surface density is a three-dimensional quantity, and it is extremely challenging to measure it experimentally. To overcome this difficulty, Shepherd [59] proposed a two-dimensional estimation of the flame surface density by a direct measurement of the flame front length and flame zone area as a function of the mean progress variable. The instantaneous flame front length as a function of the mean progress variable, $L_i(\langle c \rangle)$, was determined by dividing each instantaneous flame front into segments of one pixel length (0.0912 mm), and superimposing each flame front segment onto the contour of $\langle c \rangle$. Each flame front segment was then assigned a $\langle c \rangle$ value. The frequency distribution of the obtained values was used to determine $L_i(\langle c \rangle)$, as shown in Fig. 25(a). The flame zone area as a function
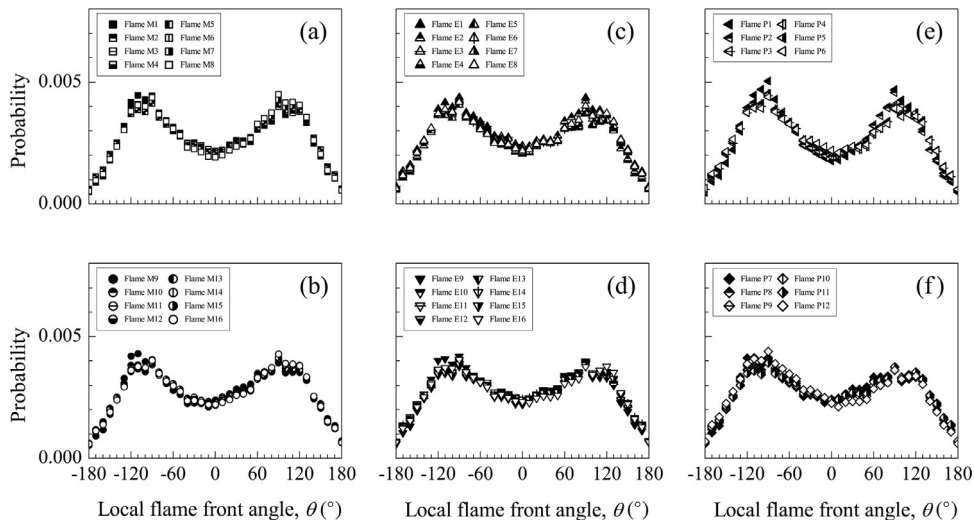

Fig. 24. Probability density functions of the local flame front angle for (a) Flames M1–M8, (b) Flames M9–M16, (c) Flames E1–E8, (d) Flames E9–E16, (e) Flames P1–P6, and (f) Flames P7–P12.
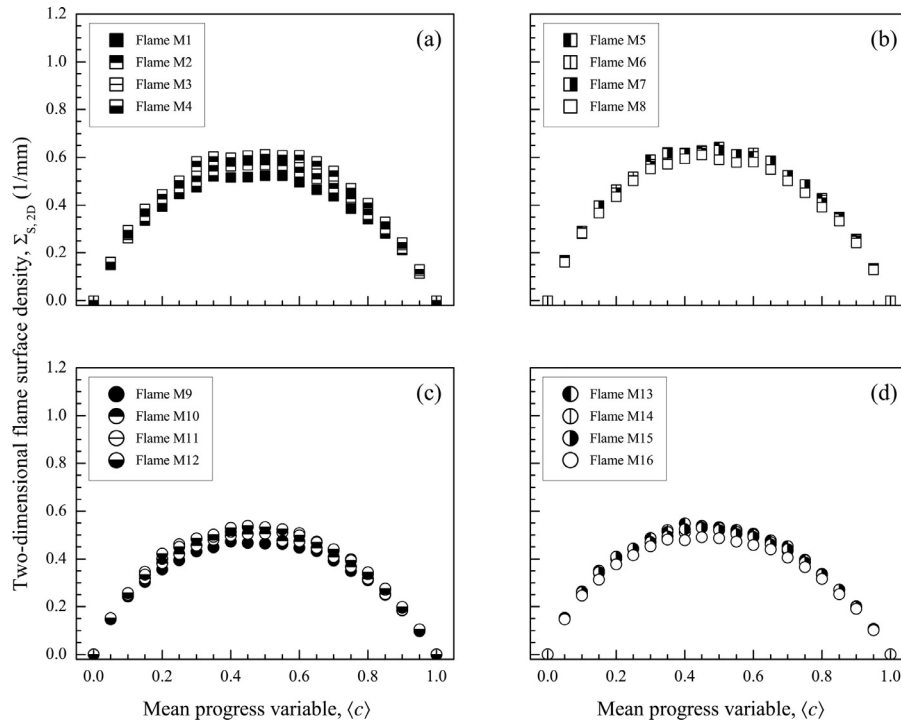
Fig. 26. Two-dimensional flame surface density profiles evaluated by the Shepherd's method with respect the mean progress variable for (a) Flames M1–M4, (b) Flames M5–M8, (c) Flames M9–M12, and (d) Flames M13–M16.

of the mean progress variable, $A(\langle c \rangle)$, was determined from the frequency distribution of $\langle c \rangle$ values obtained from $\langle c \rangle$ contour, and the area of each pixel (0.0083 mm^2) [91], as shown in Fig. 25(b). The two-dimensional flame surface density evaluated by the Shepherd's method was then obtained using the following expression [59,82,91]:

$$\Sigma_{S,2D}(\langle c \rangle) = \frac{1}{n_f} \frac{\sum_{p=1}^{n_f} L_{i,p}(\langle c \rangle)}{A(\langle c \rangle)}, \tag{10}$$

where the index S refers to the Shepherd's method, n_f is the number of flame images analyzed for each flame condition, and $L_{i,p}(\langle c \rangle)$ is the instantaneous flame front length of a flame realization p with respect to the mean progress variable.

The two-dimensional flame surface density profiles evaluated by the Shepherd's method, $\Sigma_{S,2D}$, with respect to the mean progress variable for methane/air flames, as a representative fuel type, are shown in Fig. 26(a)–(d). The shape of these profiles is similar to the previous measurements of Lachaux et al. [53], Halter et al. [73], Yuen and Gülder [33], Cohé et al. [55], and Zhang et al. [75,76] for Bunsen-type flames, Shepherd [59] for V-shaped and stagnation-point flames, and Shepherd et al. [82] for low-swirl stabilized flames. Results show that $\Sigma_{S,2D}$ increased with increasing equivalence ratio from 0.7 to 1.0, and it decreased slightly with increasing equivalence ratio from 1.1 to 1.35. This observation indicates that the flame surface density increases by increasing the unstrained premixed laminar burning velocity. The two-dimensional flame surface density evaluated by the Shepherd's method decreased by increasing the total turbulence intensity under constant equivalence ratio, non-dimensional bulk flow velocity, and non-dimensional longitudinal integral length scale, see, for example, Flames M8 and M16. The turbulent structures become smaller by increasing the total turbulence intensity which results in smaller flame surface elements, and hence an increase in the flame front wrinkling [75]. Increasing the total turbulence intensity results in an increase in the mean volume of the turbulent flame region (see Fig. 19(a)–(c)). The two-dimensional analog to the former

statement refers to an increase in the flame front length as a function of $\langle c \rangle$, and the two-dimensional analog to the latter observation represents an increase in the flame zone area as a function of $\langle c \rangle$. It seems that an increase in $A(\langle c \rangle)$ is more pronounced than an increase in $L(\langle c \rangle)$ which results in a decrease of $\Sigma_{S,2D}$ with increasing total turbulence intensity. Results show that $\Sigma_{S,2D}$ for rich mixtures was higher than the corresponding value for lean/stoichiometric mixtures under constant unstrained premixed laminar burning velocity, non-dimensional bulk flow velocity, non-dimensional turbulence intensity, and non-dimensional longitudinal integral length scale, see, for example, Flames M2 and M7. This observation may be attributed to the different thermo-diffusive characteristics of lean/stoichiometric and rich mixtures. The location of the maximum two-dimensional flame surface density evaluated by the Shepherd's method, $\Sigma_{S,2D,max}$, remained in the region between $\langle c \rangle = 0.40$ to 0.55. Experimental measurements of Yuen and Gülder [33] reported a similar observation.

It should be mentioned that the profiles of $\Sigma_{S,2D}$ with respect to the mean progress variable for ethane/– and propane/air flames are similar to methane/air flames. However, there exists one discrepancy in the trend of $\Sigma_{S,2D}$ profiles for rich mixtures. In order to demonstrate this difference, the variations of the maximum two-dimensional flame surface density evaluated by the Shepherd's method, $\Sigma_{S,2D,max}$, with respect to the equivalence ratio for all operating conditions are shown in Fig. 27(a)–(c). It is observed that $\Sigma_{S,2D,max}$ are relatively invariant with increasing equivalence ratio from 1.15 to 1.45 for ethane/air flames at high turbulence intensity, that is, Flames E13–E16, and 1.15–1.35 for propane/air flames, that is, Flames P4–P6 and Flames P10–P12. The summary of $\Sigma_{S,2D,max}$ results is tabulated in Table 3.

The two-dimensional flame surface density evaluated by the Shepherd's method normalized by its maximum value, $\Sigma_{S,2D}/\Sigma_{S,2D,max}$, with respect to the mean progress variable for all sets of experiments are shown in Fig. 28(a)–(f). It is observed that these profiles collapse, and they are not sensitive to the equivalence
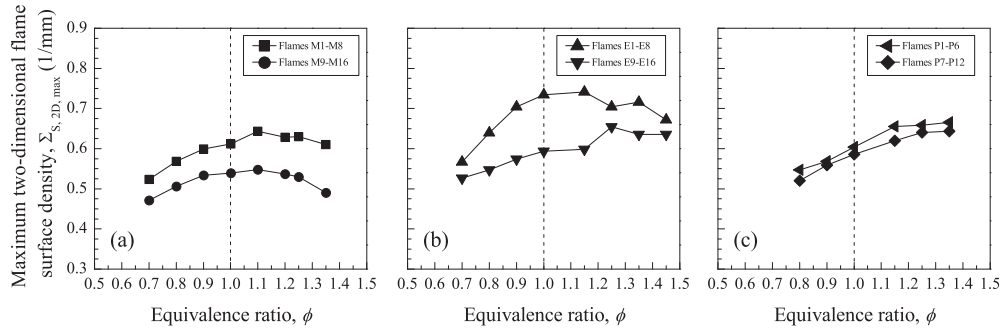
Fig. 27. Maximum two-dimensional flame surface density evaluated by the Shepherd's method with respect to the equivalence ratio for (a) methane/air, (b) ethane/air, and (c) propane/air flames.
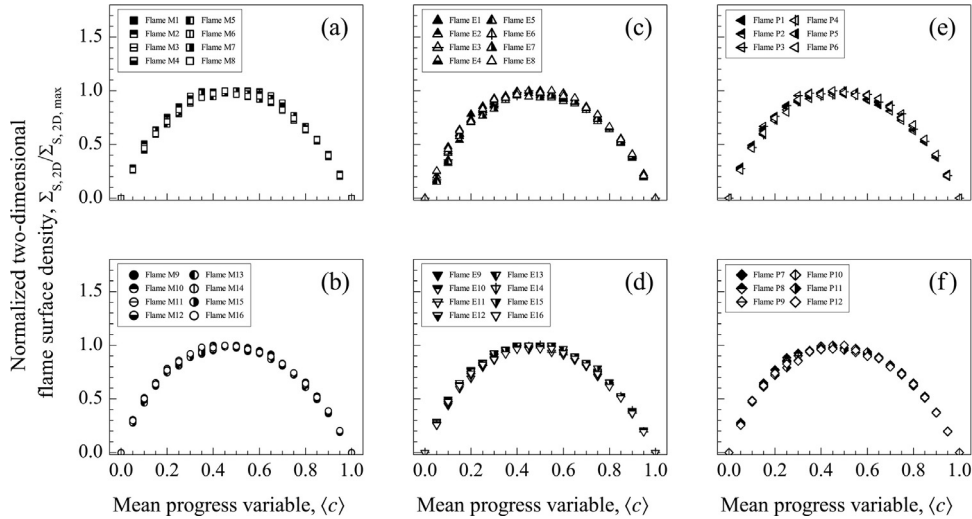

Fig. 28. Normalized two-dimensional flame surface density evaluated by the Shepherd's method for (a) Flames M1–M8, (b) Flames M9–M16, (c) Flames E1–E8, (d) Flames E9–E16, (e) Flames P1–P6, and (f) Flames P7–P12. All the profiles in this figure collapse. However, these profiles are plotted for each set of experiments in a separate subfigure for the sake of clarity.

ratio (for example, Flames M1–M8), total turbulence intensity (for example, Flames E1 and E9), different thermo-diffusive characteristics (for example, Flames P3 and P4), and the fuel type.

The flame surface density can also be characterized in the physical space. As discussed before, two methods were used to evaluate the flame surface density in the space coordinates. The first method was obtained from the mean flame front length per unit area. Following Filatyev et al. [3], the instantaneous flame front images were divided into interrogation boxes with dimensions of 2.92×1.46 mm^2. The instantaneous flame front length for each interrogation box was obtained by multiplying the number of flame front pixels into the resolution of the image. For each interrogation box, the mean value of all these lengths, which was obtained by taking an average over 500 flame front lengths, divided by the area of the interrogation box is then equal to the flame surface density of the desired region.

A contour plot of the two-dimensional flame surface density evaluated by the aforementioned method for a representative flame condition, Flame M3, is shown in Fig. 29(a). The two-dimensional flame surface density profiles at different normalized axial distances from the burner exit are shown in Fig. 29(b). As can be observed in Fig. 29(b), the two-dimensional flame surface density profile is tall and narrow near the rim of the burner at $h/D = 2$, whereas these profiles become shorter and are distributed over a larger volume farther downstream of the burner exit. Similar observations were previously reported in the literature, see, for example, Filatyev et al. [3], Bell et al. [66], Steinberg et al. [93], and Zhang et al. [75,76].

The second method which was used to evaluate the flame surface density in the space coordinates was developed by Pope [92].
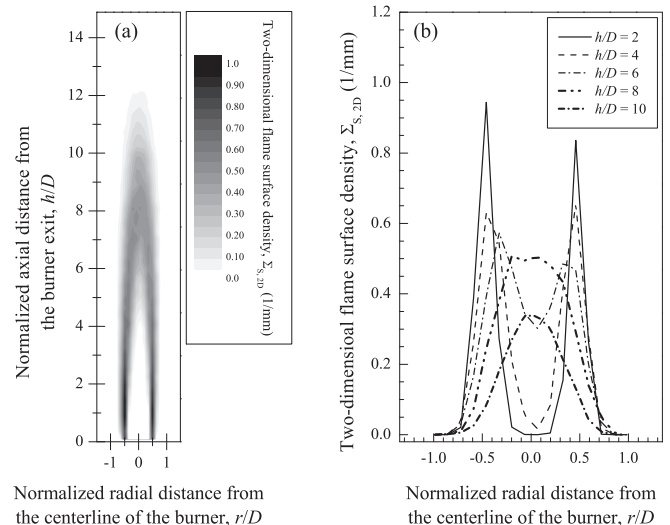

Fig. 29. (a) Contour plot of the two-dimensional flame surface density evaluated by the mean flame front length per unit area method for Flame M3 and (b) the two-dimensional flame surface density profiles using the same method with respect to the normalized radial distance from the centerline of the burner.

This method is based on calculating the gradient of the progress variable in the flame zone. In addition, Halter et al. [56] rewrote the equation proposed by Pope [92] for a Bunsen-type burner. Following Halter et al. [56], the two-dimensional flame surface
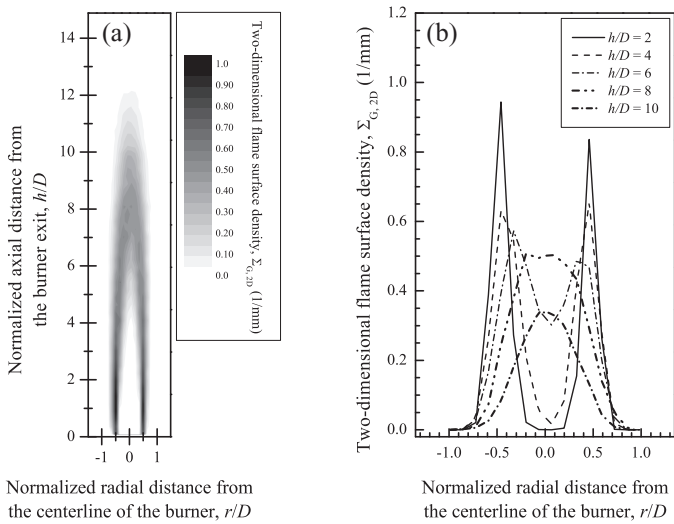
Fig. 30. (a) Contour plot of the two-dimensional flame surface density evaluated by the gradient of the progress variable method for Flame M3 and (b) the two-dimensional flame surface density profiles using the same method with respect to the normalized radial distance from the centerline of the burner.

density in the space coordinates was evaluated using the following expression:

$$\Sigma_{G,2D}(r, h) = \left\langle \left(\frac{\partial c}{\partial r} \right)^2 + \left(\frac{\partial c}{\partial h} \right)^2 \right\rangle^{\frac{1}{2}}, \tag{11}$$

where the index G refers to the gradient of the progress variable method. The instantaneous flame surface density was evaluated by calculating $\partial c/\partial r$ and $\partial c/\partial h$ for each pixel with the central differencing scheme and determining its norm. The next step was to take an average of all these values for each interrogation box. These boxes were introduced earlier in the previous method which was utilized to evaluate the flame surface density in the space coordinates. This will help to compare the flame surface density values using both methods at the same physical locations. The flame surface density for each interrogation box was then determined by taking an average over 500 data.

A contour plot of the two-dimensional flame surface density evaluated by the gradient of the progress variable method is shown in Fig. 30(a). By comparing the two-dimensional flame surface density values at different axial distances from the burner exit using both methods (see Figs. 29(b) and 30(b)), it is observed that the values are relatively similar. This observation implies that the flame surface density values in the space coordinates are identical using both methods, that is, the mean flame front length per unit area method and the gradient of the progress variable method.

3.8. Wrinkled flame surface area

Damköhler [94] hypothesized that the main effect of turbulence on the flames located in the flamelet regime is to wrinkle the reaction layers, and the flamelet consumption velocity is equal to the unstrained premixed laminar burning velocity. He stated that the ratio of the turbulent burning velocity to the unstrained premixed laminar burning velocity, S_T/S_L^0, is equal to the ratio of the wrinkled flame surface area to the unwrinkled flame surface area, A_w/A_u. The unwrinkled flame surface area, A_u, is equal to $A_{T,\langle c \rangle = 0.5}$, where the latter is the mean turbulent flame surface area conditioned at $\langle c \rangle = 0.5$ [7]. Following Griebel et al. [31], the mean turbulent flame surface conditioned at $\langle c \rangle = 0.5$ was constructed by rotating the iso-contour of $\langle c \rangle = 0.5$ around the h-axis in a virtual environment. To examine

whether the Damköhler's hypothesis is valid for the flames tested in this study, it is necessary to investigate the wrinkled flame surface area, A_w, along with the ratio of the wrinkled to the unwrinkled flame surface area, A_w/A_u. This examination will be discussed in detail in Section 3.10.

Following Driscoll [7], the wrinkled flame surface area can be obtained using the following expression:

$$A_w = \int_V \Sigma dV, \tag{12}$$

where V is the volume of the flame. As discussed in Section 3.7, the flame surface density is a three-dimensional quantity, whereas the current experimental arrangements were able to measure the two-dimensional flame surface density. In order to evaluate the three-dimensional flame surface density from the two-dimensional measurements, the information of the angle between the normal to the instantaneous flame surface and the mean flame surface, that is, crossing angle, is necessary [95]. Due to the axisymmetric nature of the flow field in a Bunsen-type burner, it is assumed that the flame front has a symmetric mean orientation with respect to its axis, and the crossing angle can be determined from images in one plane [96]. The mean direction cosine, cosine of the mean crossing angle, was reported to be 0.69 by Deschamps et al. [96], 0.55–0.65 by Chen and Bilger [97], 0.7 by Lee et al. [71], and 0.65 by Yuen and Gülder [33] for premixed turbulent Bunsen-type flames, and 0.65 by Shepherd and Ashurst [98] for premixed turbulent stagnation-point flames. Trouvé and Poinsot [99] showed that the mean direction cosine is approximately 0.7 across the turbulent flame brush using direct numerical simulation. In this study, the value of 0.65, measured by Yuen and Gülder [33] for Bunsen-type flames, was used to evaluate the three-dimensional flame surface density from the two-dimensional measurements using the following expression:

$$\Sigma = \frac{1}{|\langle \alpha_{DC} \rangle|} \Sigma_{*,2D}, \tag{13}$$

where $|\langle \alpha_{DC} \rangle|$ is the mean direction cosine, and the index $*$ can be replaced by either the Shepherd's method or the gradient of the progress variable method.

A mean direction cosine value of 0.65 suggests that the ratio of the three-dimensional to the two-dimensional wrinkled flame surface area is a constant value of 1.54. This is a promising approach for the current test conditions with the turbulent Reynolds numbers of about 140 and 340 since Chen [100] showed that the aforementioned ratio varies from 1.2 to 1.6 when the turbulent Reynolds number is less than 1000 by applying a data processing scheme on the two-sheet imaging technique. The variations of the ratio of the wrinkled to the unwrinkled flame surface area with respect to the equivalence ratio for all operating conditions are shown in Fig. 31(a)–(c). The values of A_w/A_u for each flame condition are almost similar using the Shepherd's method or the gradient of the progress variable method. This observation is expected due to the fact that the two-dimensional flame surface densities in the space coordinates evaluated with both methods are equal. The ratio of the wrinkled to the unwrinkled flame surface area decreased with increasing equivalence ratio for the first, second, and sixth sets of experiments. It is observed that this ratio shows no overall trend with increasing equivalence ratio for the third, fourth, and fifth sets of experiments. Results show that A_w/A_u increased by increasing the total turbulence intensity under constant equivalence ratio, non-dimensional bulk flow velocity, and non-dimensional longitudinal integral length scale except for Flames E3 and E11, E4 and E12, and E5 and E13. This observation indicates that increasing the total turbulence intensity results in an increase in the ratio of the wrinkled to the unwrinkled flame surface area. Results show that A_w/A_u for rich mixtures was lower than the corresponding value for
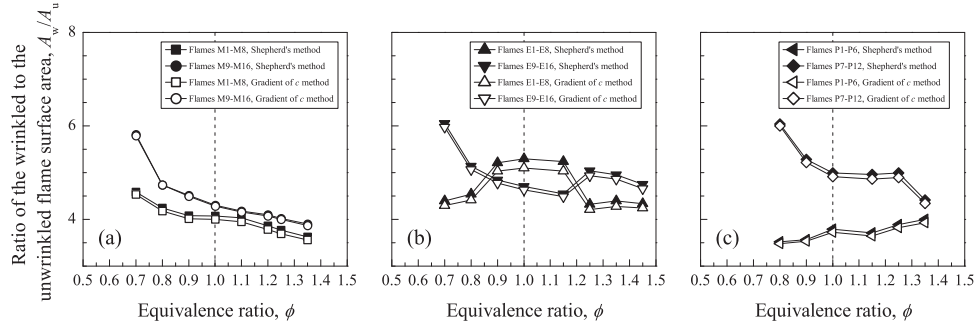
Fig. 31. Ratio of the wrinkled to the unwrinkled flame surface area with respect to the equivalence ratio for (a) methane/air, (b) ethane/air, and (c) propane/air flames. The Shepherd's method and gradient of the progress variable method were utilized to evaluate the wrinkled flame surface area.
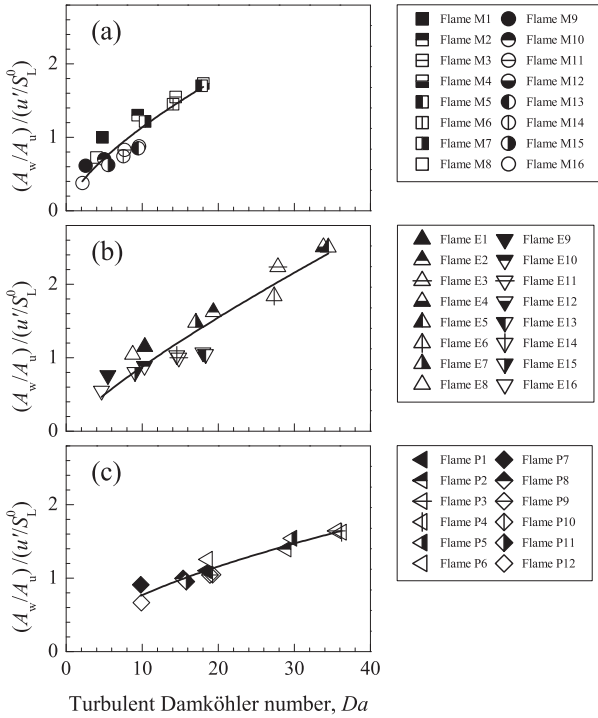

Fig. 32. Ratio of A_w/A_u to u'/S_L^0 with respect to Da for (a) methane/air (b) ethane/air, and (c) propane/air flames. It should be mentioned that the flame surface density that was utilized to evaluate A_w was estimated from the mean flame front length per unit area method. The solid line in each subfigure refers to the least-squares fit to the measured data.

lean/stoichiometric mixtures under constant S_L^0, U_B/S_L^0, u'/S_L^0, and Λ_L/δ_f except for Flames E11 and E14, P1 and P6, and P2 and P5. This trend may be attributed to the different thermo-diffusive characteristics of lean/stoichiometric and rich mixtures. The summary of A_w/A_u values for all flame conditions evaluated by the Shepherd's method and gradient of the progress variable method is tabulated in Table 3.

Fig. 32 shows that the ratio of A_w/A_u to u'/S_L^0 has a power-law relation with the turbulent Damköhler number using the following expression:

$$\frac{A_w/A_u}{u'/S_L^0} = \begin{cases} 0.24 Da^{0.67} & \text{methane/air flames,} \\ 0.13 Da^{0.82} & \text{ethane/air flames,} \\ 0.20 Da^{0.59} & \text{propane/air flames.} \end{cases} \quad (14)$$

The above equation is then converted into the following expression:

$$\frac{A_w}{A_u} = \begin{cases} 0.24\left(\frac{u'}{S_L^0}\right)^{0.33}\left(\frac{\Lambda_L}{\delta_f}\right)^{0.67} & \text{methane/air flames,} \\ 0.13\left(\frac{u'}{S_L^0}\right)^{0.18}\left(\frac{\Lambda_L}{\delta_f}\right)^{0.82} & \text{ethane/air flames,} \\ 0.20\left(\frac{u'}{S_L^0}\right)^{0.41}\left(\frac{\Lambda_L}{\delta_f}\right)^{0.59} & \text{propane/air flames.} \end{cases} \quad (15)$$

The above expression which relates the ratio of A_w/A_u to u'/S_L^0 to the turbulent Damköhler number was previously reported by Chen [100]. The formulas presented in Eqs. (14) and (15) are not valid in general since Eq. (15) does not equal to unity at $u'/S_L^0 = 0$. Chen [100] argued that the flame front wrinkling is dominated by thermo-diffusive effects for the flames operating at $u'/S_L^0 < 1$, and this kind of flames should be treated differently.

3.9. Turbulent burning velocity

As mentioned earlier, the knowledge of the turbulent burning velocity, S_T, is essential for the design of premixed turbulent combustion devices and numerical model testing [22]. The turbulent burning velocity conditioned at a specific mean progress variable, $S_{T,\langle c \rangle}$, was evaluated using the following expression [7]:

$$S_{T,\langle c \rangle} = U_B \frac{A_0}{A_{T,\langle c \rangle}}, \quad (16)$$

where $A_{T,\langle c \rangle}$ is the mean turbulent flame surface area conditioned at $\langle c \rangle$. Eq. (16) indicates that $S_{T,\langle c \rangle}$ is a function of the mean progress variable. Results show that for a representative flame condition, Flame M12, $S_{T,\langle c \rangle}/S_L^0$ decreased with increasing mean progress variable, as shown in Fig. 33. This trend was expected because of the fact that $A_{T,\langle c \rangle}$ increased with increasing mean progress variable which results in a decrease in the turbulent burning velocity, see Eq. (16). Experimental measurements of Venkateswaran et al. [101] showed a similar trend. It is observed that $S_{T,\langle c \rangle}$ is larger than S_L^0 for all $\langle c \rangle$ values.

The choice of different $\langle c \rangle$ values for determining $A_{T,\langle c \rangle}$, which results in different $S_{T,\langle c \rangle}$ values, is an arbitrary decision [7]. For example, Griebel et al. [31] used the iso-contour of $\langle c \rangle = 0.05$, Kobayashi et al. [74], Cohé et al. [54,55], and Zhang et al. [75,76] utilized the iso-contour of $\langle c \rangle = 0.1$, and Venkateswaran et al. [101,102] used the iso-contour of $\langle c \rangle = 0.5$ for determining the mean turbulent flame surface area. Tamadonfar and Gülder [24] utilized the iso-contours of $\langle c \rangle = 0.05$ and 0.5 for evaluating $A_{T,\langle c \rangle}$. All of these choices make it difficult if not impractical to compare the quantitative values of the turbulent burning velocity available in the literature. In this study, two different iso-contours of $\langle c \rangle = 0.05$ and 0.5, similar to [24], were utilized to evaluate the burning velocity of premixed turbulent
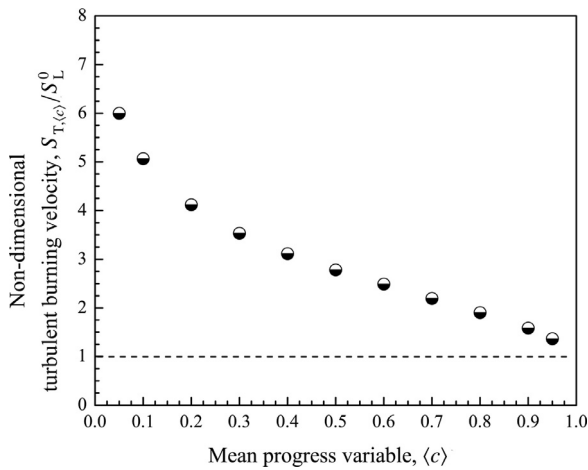
Fig. 33. Non-dimensional turbulent burning velocity with respect to the mean progress variable for Flame M12.
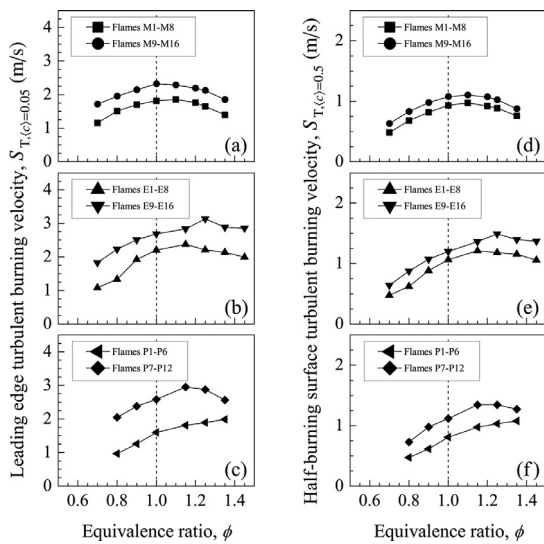

Fig. 34. Leading edge turbulent burning velocity for (a) methane/air, (b) ethane/air, and (c) propane/air flames, and half-burning surface turbulent burning velocity for (d) methane/air, (e) ethane/air, and (f) propane/air flames with respect to the equivalence ratio.

flames. The burning velocity which used the iso-contour of $\langle c \rangle = 0.05$ represents the leading edge turbulent burning velocity, and the one which utilized the iso-contour of $\langle c \rangle = 0.5$ refers to the half-burning surface turbulent burning velocity.

The variations of the leading edge and half-burning surface turbulent burning velocities for all operating conditions with respect to the equivalence ratio are shown in Fig. 34(a)–(c) and (d)–(f), respectively. The qualitative trends of the leading edge and half-burning surface turbulent burning velocities with respect to the equivalence ratio are found to be similar. Results show that the leading edge and half-burning surface turbulent burning velocities increased with increasing equivalence ratio from lean to stoichiometric mixtures for methane/–, ethane/–, and propane/air flames, whereas they decreased with increasing equivalence ratio for rich mixtures except for Flames E13–E16 and P4–P6. Experimental measurements of Shy et al. [14] displayed a similar trend for downward propagating premixed turbulent methane/air flames. This trend indicates that, in general, increasing the unstrained premixed laminar burning velocity results in an increase in the turbulent burning velocity when the turbulence statistics were kept constant. Results show that the leading edge and half-burning surface turbulent burning velocities increased

with increasing total turbulence intensity when the equivalence ratio, non-dimensional bulk flow velocity, and non-dimensional longitudinal integral length scale were kept constant. For example, the leading edge turbulent burning velocity is equal to 1.08 m/s for Flame E1, and it increases to 1.83 m/s for Flame E9 by a two-fold increase in the total turbulence intensity. Similar observations were previously reported for premixed turbulent Bunsen flames, see, for example, [24,103], propagating flame kernels, see, for example, [17], and downward propagating premixed turbulent flames, see, for example, [14]. This observation may be attributed to an increase in the local flame surface area with turbulent structures [94]. Results show that the leading edge and half-burning surface turbulent burning velocities for rich mixtures were larger than the corresponding values for lean/stoichiometric mixtures under constant unstrained premixed laminar burning velocity, non-dimensional bulk flow velocity, non-dimensional turbulence intensity, and non-dimensional longitudinal integral length scale. For example, the leading edge and half-burning surface turbulent burning velocities for Flame E11 are equal to 2.51 and 1.07 m/s, respectively, and they increase to 3.14 and 1.49 m/s for Flame E14. This difference may be attributed to the different thermo-diffusive characteristics of lean/stoichiometric and rich mixtures. On the other hand, Shy et al. [14] showed that the burning velocity of downward propagating premixed turbulent flames for lean/stoichiometric mixtures is higher than the corresponding value for rich mixtures under constant unstrained premixed laminar burning velocity, non-dimensional turbulence intensity, and non-dimensional longitudinal integral length scale.

The values of the leading edge and half-burning surface turbulent burning velocities for all flame conditions are tabulated in Table 4. The ratio of the leading edge to the half-burning surface turbulent burning velocity, $S_{T,\langle c \rangle = 0.05}/S_{T,\langle c \rangle = 0.5}$, changed from 1.84 to 2.84, see Table 4. A similar observation was previously reported in [24], whereas Smallwood et al. [52] proposed that this ratio varies from 1.2 to 1.5 for premixed turbulent Bunsen flames. As discussed in [24], this difference may be attributed to the different methods utilized for evaluating the mean turbulent flame surface area and different ranges of non-dimensional turbulence intensity tested. A comparison between the characteristic flame height values in Table 3 and the turbulent burning velocity data in Table 4 demonstrated that the characteristic flame height is inversely proportional to the turbulent burning velocity. This dependence was previously reported in [24].

There has been a discussion in the combustion community about the largest value of non-dimensional burning velocity of premixed turbulent flames, S_T/S_L^0, that can be achieved [7]. The maximum values of the non-dimensional leading edge turbulent burning velocity, $S_{T,\langle c \rangle = 0.05}/S_L^0$, and non-dimensional half-burning surface turbulent burning velocity, $S_{T,\langle c \rangle = 0.5}/S_L^0$, in this study belong to Flame E16, and they are equal to 13.1 and 6.3, respectively. A similar observation was previously reported by Yuen and Gülder [87] for premixed turbulent methane/air Bunsen flames. Venkateswaran et al. [101] and Daniele et al. [25] showed that the maximum values of the non-dimensional half-burning surface turbulent burning velocity for lean syngas/air flames were about 42.5 at atmospheric condition and 46 at 5 atmospheres, respectively.

3.10. Mean turbulent flame stretch factor

As discussed in Section 3.8, Damköhler [94] hypothesized that the non-dimensional turbulent burning velocity is equal to the ratio of the wrinkled to the unwrinkled flame surface area. The half-burning surface turbulent burning velocity was utilized in investigating the Damköhler's hypothesis [7]. The non-dimensional half-burning surface turbulent burning velocity with respect to the ratio of the wrinkled to the unwrinkled flame surface area for all experimental conditions is shown in Fig. 35. It is observed that A_w/A_u is significantly larger than $S_{T,\langle c \rangle = 0.5}/S_L^0$ for the majority of flame

Table 4

Summary of experimental results. Symbols: ϕ = equivalence ratio; U_B = bulk flow velocity; u' = total turbulence intensity; S_L^0 = unstrained premixed laminar burning velocity; Λ_L = longitudinal integral length scale; δ_f = Zel'dovich thickness; $S_{T,\langle c\rangle=0.05}$ = leading edge turbulent burning velocity; $S_{T,\langle c\rangle=0.5}$ = half-burning surface turbulent burning velocity; $\langle S_L\rangle$ = mean flamelet consumption velocity; $\langle I_0\rangle$ = mean turbulent flame stretch factor.

Set of exp.	Flame	ϕ (–)	U_B/S_L^0 (–)	u'/S_L^0 (–)	Λ_L/δ_f (–)	$S_{T,\langle c\rangle=0.05}$ (m/s)	$S_{T,\langle c\rangle=0.5}$ (m/s)	$S_{T,\langle c\rangle=0.05}/S_{T,\langle c\rangle=0.5}$ (–)	$\langle S_L\rangle$ (m/s)	$\langle I_0\rangle$ (–)
I	M1	0.7	105.7	4.6	21.8	1.16	0.48	2.40	0.11	0.53
	M2	0.8	75.1	3.3	30.6	1.51	0.68	2.22	0.16	0.57
	M3	0.9	60.7	2.6	37.9	1.70	0.82	2.08	0.20	0.58
	M4	1.0	54.3	2.4	42.4	1.82	0.93	1.94	0.23	0.59
	M5	1.1	54.6	2.4	42.2	1.86	0.98	1.91	0.24	0.63
	M6	1.2	61.5	2.7	37.5	1.76	0.92	1.90	0.24	0.70
	M7	1.25	71.6	3.1	32.2	1.64	0.89	1.85	0.24	0.80
	M8	1.35	115.6	5.0	19.9	1.40	0.76	1.85	0.21	1.15
II	M9	0.7	105.7	9.5	24.1	1.71	0.63	2.72	0.11	0.55
	M10	0.8	75.1	6.8	33.8	1.95	0.83	2.35	0.18	0.63
	M11	0.9	60.7	5.5	41.9	2.14	0.98	2.18	0.22	0.63
	M12	1.0	54.3	4.9	46.8	2.32	1.08	2.16	0.25	0.65
	M13	1.1	54.6	4.9	46.6	2.28	1.10	2.07	0.26	0.69
	M14	1.2	61.5	5.5	41.4	2.19	1.07	2.04	0.26	0.77
	M15	1.25	71.6	6.4	35.5	2.12	1.02	2.07	0.25	0.87
	M16	1.35	115.6	10.4	22.0	1.85	0.87	2.11	0.22	1.23
III	E1	0.7	88.2	3.8	39.5	1.08	0.47	2.28	0.11	0.45
	E2	0.8	64.5	2.8	54.1	1.33	0.62	2.14	0.14	0.42
	E3	0.9	53.7	2.3	64.8	1.92	0.88	2.17	0.17	0.43
	E4	1.0	48.8	2.1	71.5	2.20	1.06	2.07	0.20	0.47
	E5	1.15	48.3	2.1	72.2	2.37	1.21	1.96	0.23	0.53
	E6	1.25	54.2	2.3	64.3	2.21	1.18	1.87	0.27	0.71
	E7	1.35	68.7	3.0	50.8	2.13	1.16	1.85	0.26	0.86
	E8	1.45	95.9	4.2	36.3	1.99	1.06	1.89	0.24	1.11
IV	E9	0.7	88.2	7.9	43.7	1.83	0.64	2.84	0.11	0.45
	E10	0.8	64.5	5.8	59.7	2.23	0.88	2.54	0.17	0.52
	E11	0.9	53.7	4.8	71.6	2.51	1.07	2.34	0.22	0.57
	E12	1.0	48.8	4.4	78.9	2.69	1.20	2.23	0.26	0.59
	E13	1.15	48.3	4.3	79.7	2.84	1.37	2.08	0.30	0.69
	E14	1.25	54.2	4.9	71.0	3.14	1.49	2.10	0.30	0.77
	E15	1.35	68.7	6.2	56.1	2.88	1.40	2.06	0.28	0.92
	E16	1.45	95.9	8.6	40.1	2.86	1.37	2.08	0.29	1.32
V	P1	0.8	73.8	3.2	59.1	0.96	0.47	2.04	0.13	0.47
	P2	0.9	59.0	2.6	74.0	1.26	0.61	2.04	0.17	0.48
	P3	1.0	53.2	2.3	82.0	1.60	0.81	1.98	0.21	0.54
	P4	1.15	52.7	2.3	82.8	1.81	0.97	1.86	0.26	0.66
	P5	1.25	58.2	2.5	74.9	1.89	1.03	1.84	0.26	0.73
	P6	1.35	73.6	3.2	59.3	1.98	1.08	1.84	0.27	0.94
VI	P7	0.8	73.8	6.6	65.3	2.04	0.73	2.81	0.12	0.42
	P8	0.9	59.0	5.3	81.7	2.38	0.98	2.43	0.19	0.52
	P9	1.0	53.2	4.8	90.6	2.58	1.12	2.31	0.22	0.57
	P10	1.15	52.7	4.7	91.4	2.95	1.34	2.19	0.27	0.68
	P11	1.25	58.2	5.2	82.8	2.88	1.35	2.14	0.27	0.75
	P12	1.35	73.6	6.6	65.5	2.56	1.27	2.01	0.29	1.01

conditions. On the other hand, the measurements of Chen and Bilger [97] displayed that the ratio of the wrinkled to the unwrinkled flame surface area is smaller than the non-dimensional turbulent burning velocity. It can be concluded that the Damköhler's hypothesis is not valid for the flames tested in this and previous studies [97]. This means that the flamelet consumption velocity is not equal to the unstrained premixed laminar burning velocity. However, Haworth and Poinsot [104], Bell et al. [105], and Hawkes and Chen [106] validated the Damköhler's hypothesis by investigating the premixed turbulent flames using DNS.

In order to evaluate the mean flamelet consumption velocity, Driscoll [7] showed that the ratio of the half-burning surface turbulent burning velocity to the unstrained premixed laminar burning velocity can be formulated using the following expression:

$$\frac{S_{T,\langle c\rangle=0.5}}{S_L^0} = \frac{\langle S_L\rangle}{S_L^0}\frac{A_w}{A_u} = \langle I_0\rangle\frac{A_w}{A_u}, \tag{17}$$

where $\langle S_L\rangle$ is the mean flamelet consumption velocity, and $\langle I_0\rangle$ is the mean turbulent flame stretch factor (averaged in time and space).

The contour of the mean progress variable, iso-contour of $\langle c\rangle = 0.5$, and instantaneous flame front locations are shown in Fig. 36(a) and (b). To clarify the definition of mean flamelet consumption velocity, Fig. 36(b) shows the latter parameter along with the definition of half-burning surface turbulent burning velocity. According to Eq. (17), $\langle I_0\rangle$ is the ratio of the mean flamelet consumption velocity to the unstrained premixed laminar burning velocity. The variations of the mean turbulent flame stretch factor with respect to the equivalence ratio for all experimental conditions are shown in Fig. 37(a)–(c). Results show that $\langle I_0\rangle$ increased significantly with increasing equivalence ratio for each set of experiments. It is observed that the values of $\langle I_0\rangle$ are smaller than 1.0 for all flame conditions except for Flames M8, M16, E8, E16, and P12. This observation indicates that the mean flamelet consumption velocity is smaller than the unstrained premixed laminar burning velocity except for the aforementioned test conditions. Halter et al. [56] did not report the mean turbulent flame stretch factor directly, and they reported the inverse of this quantity. Their results showed that the inverse of the mean turbulent flame stretch factors are higher than 1.0 for lean premixed turbulent Bunsen flames at atmospheric condition using the same
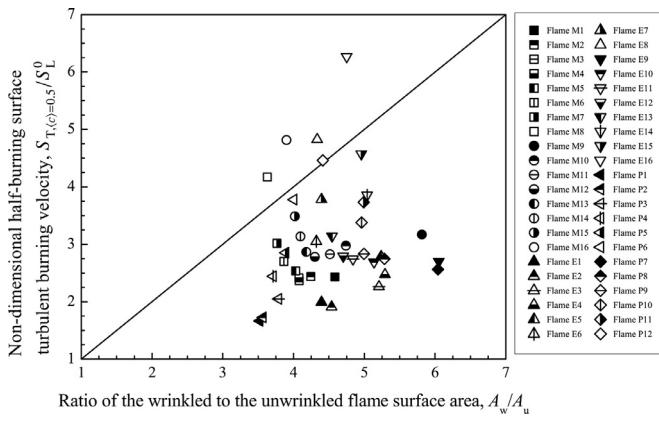
Fig. 35. Non-dimensional half-burning surface turbulent burning velocity with respect to the ratio of the wrinkled to the unwrinkled flame surface area. The solid line indicates the Damköhler's hypothesis.
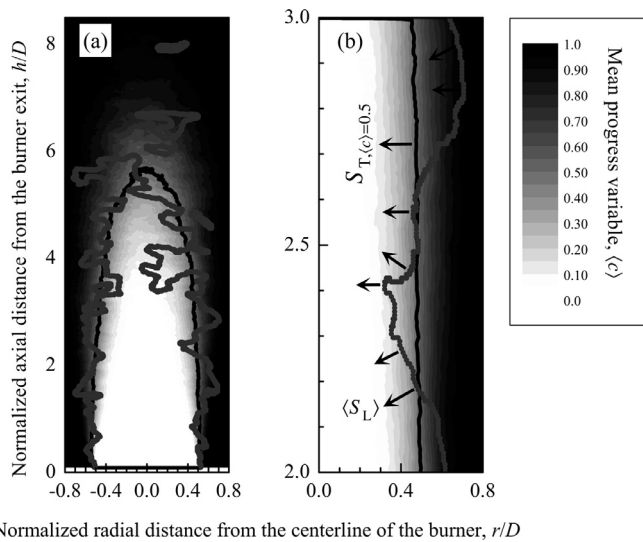

Fig. 36. (a) and (b) show the mean progress variable contour, iso-contour of $\langle c \rangle = 0.5$ (black line), and instantaneous flame front locations (gray line) for Flame M12. The definitions of $S_{T,\langle c \rangle = 0.5}$ and $\langle S_L \rangle$ are shown in (b).

method utilized in this study. This means that $\langle I_0 \rangle$ values are less than 1.0 for these flame conditions. On the other hand, Troiani et al. [81] showed that the mean turbulent flame stretch factor varies from 1.10 to 1.94 for premixed turbulent methane/air Bunsen flames. Experimental measurements of Daniele et al. [25] showed that the ratio of the mean flamelet consumption velocity to the unstained premixed laminar burning velocity varies between approximately 1.0 and 8.5 for premixed turbulent flames at high pressure and temperature. Lin et al. [107] reported that the aforementioned ratio changes

between approximately 2.0 and 23.0 for premixed turbulent flames at high pressure and temperature. Results show that $\langle I_0 \rangle$ increased with increasing total turbulence intensity when the equivalence ratio, non-dimensional bulk flow velocity, and non-dimensional longitudinal integral length scale were kept constant. For example, $\langle I_0 \rangle$ evaluated by the Shepherd's method is equal to 0.47 for Flame E4, and it increases to 0.59 for Flame E12. This observation indicates that the mean flamelet consumption velocity increased with increasing total turbulence intensity under constant ϕ, U_B/S_L^0, and Λ_L/δ_f. Therefore, it can be concluded that increasing the total turbulence intensity results in an increase of both mean flamelet consumption velocity and the ratio of the wrinkled to the unwrinkled flame surface area (see Figs. 31 and 37). It is observed that $\langle I_0 \rangle$ for rich mixtures is higher than the corresponding value for lean/stoichiometric mixtures when the unstrained premixed laminar burning velocity, non-dimensional bulk flow velocity, non-dimensional turbulence intensity, and non-dimensional longitudinal integral length scale were kept constant. For example, $\langle I_0 \rangle$ evaluated by the gradient of c method is equal to 0.49 for Flame P2, and it increases to 0.75 for Flame P5. This difference may be attributed to the different thermo-diffusive characteristics of lean/stoichiometric and rich mixtures. This observation suggests that the mean flamelet consumption velocity for rich mixtures is larger than the corresponding value for lean/stoichiometric mixtures when S_L^0, U_B/S_L^0, u'/S_L^0, and Λ_L/δ_f were kept constant. It should be mentioned that both the Shepherd's method and gradient of c method result in equal values for $\langle S_L \rangle$ and $\langle I_0 \rangle$. As a result, only the values of $\langle S_L \rangle$ and $\langle I_0 \rangle$ evaluated by the Shepherd's method are summarized in Table 4. It can be concluded from the data reported in Table 4 that the flame condition with a higher value of the mean flamelet consumption velocity has a larger value of the turbulent burning velocity for each set of experiments.

4. Concluding remarks

The effects of the equivalence ratio, turbulence intensity, and different thermo-diffusive characteristics on the flame brush characteristics, instantaneous flame front structures, and burning velocities of premixed turbulent methane/–, ethane/–, and propane/air Bunsen flames were investigated experimentally. The turbulence statistics and flame front corrugations were measured using the particle image velocimetry and Mie scattering techniques, respectively. Experiments were performed under a constant bulk flow velocity of 21.0 m/s. The equivalence ratio was varied from 0.7 to 1.35 for methane/air flames, 0.7–1.45 for ethane/air flames, and 0.8–1.35 for propane/air flames. The total turbulence intensity was controlled by two different perforated plates mounted upstream of the burner exit. In this study, a series of comprehensive parameters including the characteristic flame height, mean flame brush thickness, mean volume of the turbulent flame region, mean fuel consumption rate, two-dimensional flame front curvature, local flame front angle, two-dimensional flame surface density, wrinkled flame surface area, turbulent burning velocity, mean flamelet consumption velocity, and mean turbulent flame
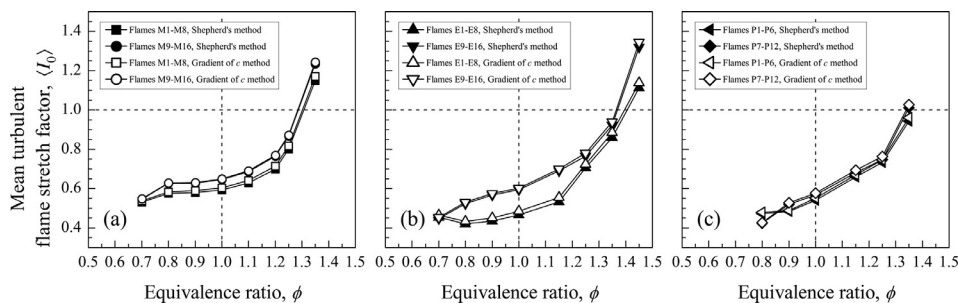

Fig. 37. Mean turbulent flame stretch factor with respect to the equivalence ratio for (a) methane/air, (b) ethane/air, and (c) propane/air flames.

stretch factor were obtained from the Mie scattering images. The key findings are summarized as follows:

1. The normalized characteristic flame height decreased with increasing equivalence ratio from lean to stoichiometric mixtures for all hydrocarbon/air flames tested in this study. It remained relatively constant with increasing equivalence ratio from 1.15 to 1.45 for ethane/air flames and 1.15–1.35 for propane/air flames, whereas it increased slightly with increasing equivalence ratio from 1.1 to 1.35 for methane/air flames. The normalized characteristic flame height decreased with increasing total turbulence intensity when the equivalence ratio, non-dimensional bulk flow velocity, and non-dimensional longitudinal integral length scale were kept constant. The normalized characteristic flame height for lean/stoichiometric mixture was higher than the corresponding value for rich mixtures under identical unstrained premixed laminar burning velocity, non-dimensional bulk flow velocity, non-dimensional turbulence intensity, and non-dimensional longitudinal integral length scale. Results show that the product of normalized characteristic flame height and turbulent Karlovitz number has a power-law relation with the turbulent Damköhler number.

2. The normalized centerline mean flame brush thickness decreased with increasing equivalence ratio from lean to stoichiometric mixtures, whereas it remained relatively constant with increasing equivalence ratio for rich mixtures. The normalized centerline mean flame brush thickness decreased with increasing total turbulence intensity when the equivalence ratio, non-dimensional bulk flow velocity, and non-dimensional longitudinal integral length scale were kept constant. The normalized centerline mean flame brush thickness for lean/stoichiometric mixtures was higher than the corresponding value for rich mixtures with identical unstrained premixed laminar burning velocity, non-dimensional bulk flow velocity, non-dimensional turbulence intensity, and non-dimensional longitudinal integral length scale. The product of normalized centerline mean flame brush thickness and turbulent Karlovitz number follows a power-law relation with the turbulent Damköhler number.

3. The normalized horizontal mean flame brush thickness increased with increasing normalized axial distance from the burner exit. It increased with increasing equivalence ratio from 0.7 to 1.0 for methane/– and ethane/air flames, and 0.8–1.0 for propane/air flames. It decreased with increasing equivalence ratio from 1.1 to 1.35 for methane/air flames, whereas it remained relatively constant with increasing equivalence ratio from 1.15 to 1.45 and 1.15–1.35 for ethane/– and propane/air flames, respectively. For all hydrocarbon/air flames, increasing the total turbulence intensity results in an increase in the normalized horizontal mean flame brush thickness under constant equivalence ratio, non-dimensional bulk flow velocity, and non-dimensional longitudinal integral length scale. The normalized horizontal mean flame brush thicknesses at different normalized axial distances from the burner exit were relatively similar for lean/stoichiometric and rich methane/air flames. The normalized horizontal mean flame brush thickness for very rich ethane/air flames was larger than the corresponding value for very lean ethane/air flames at an identical normalized axial distance from the burner exit, whereas these thicknesses were approximately equal for near stoichiometric ethane/air flames under constant unstrained premixed laminar burning velocity, non-dimensional bulk flow velocity, non-dimensional turbulence intensity, and non-dimensional longitudinal integral length scale. For propane/air flames, the behavior of these thicknesses for lean/stoichiometric and rich mixtures at low turbulence intensity was the same as ethane/air flames, whereas these thicknesses were relatively similar for lean/stoichiometric and rich mixtures at high turbulence intensity

under constant unstrained premixed laminar burning velocity, non-dimensional bulk flow velocity, non-dimensional turbulence intensity, and non-dimensional longitudinal integral length scale.

4. The mean progress variable profiles on the centerline and normal to the centerline of the burner mimicked the behavior of the complementary error function. These profiles collapsed to a universal curve when the centerline (horizontal) distance across the flame brush was normalized by the centerline (local horizontal) mean flame brush thickness.

5. The mean volume of the turbulent flame region decreased with increasing equivalence ratio from lean to stoichiometric mixtures for all hydrocarbon/air flames tested in this study. It stayed constant with increasing equivalence ratio from 1.15 to 1.45 for ethane/air flames and 1.15–1.35 for propane/air flames, whereas it increased moderately with increasing equivalence ratio from 1.1 to 1.35 for methane/air flames. The mean volume of the turbulent flame region increased with increasing total turbulence intensity under constant equivalence ratio, non-dimensional bulk flow velocity, and non-dimensional longitudinal integral length scale. The mean volume of the turbulent flame region for lean/stoichiometric mixtures was higher than the corresponding value for rich mixtures when the unstrained premixed laminar burning velocity, non-dimensional bulk flow velocity, non-dimensional turbulence intensity, and non-dimensional longitudinal integral length scale were kept constant.

6. The mean fuel consumption rate increased with increasing equivalence ratio from lean to stoichiometric mixtures for all hydrocarbon/air flames tested in the current study. It increased with increasing equivalence ratio for rich propane/air flames, whereas it remained relatively constant with increasing equivalence ratio for rich methane/– and ethane/air flames. The mean fuel consumption rate decreased with increasing total turbulence intensity under constant equivalence ratio, non-dimensional bulk flow velocity, and non-dimensional longitudinal integral length scale. The mean fuel consumption rate for rich mixtures was larger than the corresponding value for lean/stoichiometric mixtures when the unstrained premixed laminar burning velocity, non-dimensional bulk flow velocity, non-dimensional turbulence intensity, and non-dimensional longitudinal integral length scale were kept constant.

7. The flame front curvature distribution was Gaussian, and it was symmetrical about the zero flame front curvature. The flame front curvature distributions were not sensitive to the equivalence ratio, total turbulence intensity, different thermo-diffusive characteristics, and the fuel type.

8. The local flame front angle distribution was bimodal with its peak values located at $\pm 90°$. The local flame front angle distributions were not sensitive to the equivalence ratio, total turbulence intensity, different thermo-diffusive characteristics, and the fuel type.

9. The maximum two-dimensional flame surface density evaluated by the Shepherd's method increased with increasing equivalence ratio from lean to stoichiometric mixtures for all hydrocarbon/air flames tested in this study. It decreased slightly with increasing equivalence ratio for rich ethane/air flames at low turbulence intensity and rich methane/air flames, whereas it remained unaltered for rich ethane/air flames at high turbulence intensity and rich propane/air flames. The maximum two-dimensional flame surface density decreased with increasing total turbulence intensity under constant equivalence ratio, non-dimensional bulk flow velocity, and non-dimensional longitudinal integral length scale. The maximum two-dimensional flame surface density for rich mixtures was higher than the corresponding value for lean/stoichiometric mixtures when the unstrained premixed laminar burning velocity, non-dimensional bulk flow velocity, non-dimensional turbulence intensity, and non-dimensional longitudinal integral length scale were kept constant.

10. The ratio of the wrinkled to the unwrinkled flame surface area decreased with increasing equivalence ratio for propane/air flames at high turbulence intensity and methane/air flames, whereas it did not show any trend with increasing equivalence ratio for propane/air flames at low turbulence intensity and ethane/air flames. In general, this ratio increased with increasing total turbulence intensity under constant equivalence ratio, non-dimensional bulk flow velocity, and non-dimensional longitudinal integral length scale. The ratio of the wrinkled to the unwrinkled flame surface area for lean/stoichiometric mixtures was higher than the corresponding value for rich mixtures. It is observed that the ratio of the wrinkled to the unwrinkled flame surface area divided by the non-dimensional turbulence intensity has a power-law relation with the turbulent Damköhler number.

11. In general, the leading edge and half-burning surface turbulent burning velocities increased with increasing equivalence ratio from lean to stoichiometric mixtures, whereas they decreased with increasing equivalence ratio for rich mixtures. These velocities were enhanced with increasing total turbulence intensity when the equivalence ratio, non-dimensional bulk flow velocity, and non-dimensional longitudinal integral length scale were kept constant. The leading edge and half-burning surface turbulent burning velocities for lean/stoichiometric mixtures were smaller than the corresponding values for rich mixtures under constant unstrained premixed laminar burning velocity, non-dimensional bulk flow velocity, non-dimensional turbulence intensity, and non-dimensional longitudinal integral length scale.

12. The mean flamelet consumption velocity and mean turbulent flame stretch factor were derived for all experimental conditions. The mean turbulent flame stretch factor increased with increasing equivalence ratio. It also increased by increasing the total turbulence intensity under constant equivalence ratio, non-dimensional bulk flow velocity, and non-dimensional longitudinal integral length scale. Results show that this parameter for rich mixtures was larger than the corresponding value for lean/stoichiometric mixtures when the unstrained premixed laminar burning velocity, non-dimensional bulk flow velocity, non-dimensional turbulence intensity, and non-dimensional longitudinal integral length scale were kept constant.

Acknowledgments

References

[1] N. Peters, Turbulent Combustion, Cambridge University Press, 2000.
[2] R.K. Cheng, I.G. Shepherd, The influence of burner geometry on premixed turbulent flame propagation, Combust. Flame 85 (1991) 7–26.
[3] S.A. Filatyev, J.F. Driscoll, C.D. Carter, J.M. Donbar, Measured properties of turbulent premixed flames for model assessment, including burning velocities, stretch rates, and surface densities, Combust. Flame 141 (2005) 1–21.
[4] R.W. Bilger, S.B. Pope, K.N.C. Bray, J.F. Driscoll, Paradigms in turbulent combustion research, Proc. Combust. Inst. 30 (2005) 21–42.
[5] R.G. Abdel-Gayed, D. Bradley, A two-eddy theory of premixed turbulent flame propagation, Phil. Trans. R. Soc. London A 301 (1981) 1–25.
[6] R.G. Abdel-Gayed, K.J. Al-Khishali, D. Bradley, Turbulent burning velocities and flame straining in explosions, Proc. R. Soc. London A 391 (1984) 393–414.
[7] J.F. Driscoll, Turbulent premixed combustion: Flamelet structure and its effect on turbulent burning velocities, Prog. Energy Combust. Sci. 34 (2008) 91–134.
[8] A.S. Sokolik, V.P. Karpov, E.S. Semenov, Turbulent combustion of gases, Combust. Explos. Shock Waves 3 (1967) 36–45.
[9] V.P. Karpov, E.S. Severin, Effects of molecular-transport coefficients on the rate of turbulent combustion, Combust. Explos. Shock Waves 16 (1980) 41–46.
[10] D. Bradley, How fast can we burn? Proc. Combust. Inst. 25 (1992) 247–262.
[11] J.M. Duclos, D. Veynante, T. Poinsot, A comparison of flamelet models for premixed turbulent combustion, Combust. Flame 95 (1993) 101–117.
[12] R.C. Aldredge, V. Vaezi, P.D. Ronney, Premixed-flame propagation in turbulent Taylor–Couette flow, Combust. Flame 115 (1998) 395–405.
[13] N. Peters, The turbulent burning velocity for large-scale and small-scale turbulence, J. Fluid Mech. 384 (1999) 107–132.
[14] S.S. Shy, W.J. Lin, J.C. Wei, An experimental correlation of turbulent burning velocities for premixed turbulent methane–air combustion, Proc. R. Soc. London A 456 (2000) 1997–2019.
[15] H. Kido, M. Nakahara, K. Nakashima, J. Hashimoto, Influence of local flame displacement velocity on turbulent burning velocity, Proc. Combust. Inst. 29 (2002b) 1855–1861.
[16] H. Kobayashi, K. Seyama, H. Hagiwara, Y. Ogami, Burning velocity correlation of methane/air turbulent premixed flames at high pressure and high temperature, Proc. Combust. Inst. 30 (2005) 827–834.
[17] M. Fairweather, M.P. Ormsby, C.G.W. Sheppard, R. Woolley, Turbulent burning rates of methane and methane–hydrogen mixtures, Combust. Flame 156 (2009) 780–790.
[18] H. Kido, M. Nakahara, J. Hashimoto, D. Barat, Turbulent burning velocities of two-component fuel mixtures of methane, propane and hydrogen, JSME Int. J. B 45 (2002a) 355–362.
[19] M. Nakahara, T. Shirasuna, J. Hashimoto, Experimental study on local flame properties of hydrogen added hydrocarbon premixed turbulent flames, J. Therm. Sci. Technol. Jpn. 4 (2009) 190–201.
[20] R.G. Abdel-Gayed, D. Bradley, M. Lawes, Turbulent burning velocities: A general correlation in terms of straining rates, Proc. R. Soc. London A 414 (1987) 389–413.
[21] Ö. L. Gülder, Turbulent premixed flame propagation models for different combustion regimes, Proc. Combust. Inst. 23 (1990) 743–750.
[22] A.N. Lipatnikov, J. Chomiak, Turbulent flame speed and thickness: phenomenology, evaluation, and application in multi-dimensional simulations, Prog. Energy Combust. Sci. 28 (2002) 1–74.
[23] A.N. Lipatnikov, J. Chomiak, Molecular transport effects on turbulent flame propagation and structure, Prog. Energy Combust. Sci. 31 (2005) 1–73.
[24] P. Tamadonfar, Ö. L. Gülder, Flame brush characteristics and burning velocities of premixed turbulent methane/air Bunsen flames, Combust. Flame 161 (2014) 3154–3165.
[25] S. Daniele, J. Mantzaras, P. Jansohn, A. Denisov, K. Boulouchos, Flame front/turbulence interaction for syngas fuels in the thin reaction zones regime: turbulent and stretched laminar flame speeds at elevated pressures and temperatures, J. Fluid Mech. 724 (2013) 36–68.
[26] F.T.C. Yuen, Experimental Investigation of the Dynamics and Structure of Lean-premixed Turbulent Combustion, University of Toronto Institute for Aerospace Studies, 2009 (Ph.D. thesis).
[27] Ö. L. Gülder, G.J. Smallwood, R. Wong, D.R. Snelling, R. Smith, B.M. Deschamps, J.C. Sautet, Flame front surface characteristics in turbulent premixed propane/air combustion, Combust. Flame 120 (2000) 407–416.
[28] Y.C. Chen, R.W. Bilger, Simultaneous 2-D imaging measurements of reaction progress variable and OH radical concentration in turbulent premixed flames: Experimental methods and flame brush structure, Combust. Sci. Technol. 167 (2001) 131–167.
[29] H. Kobayashi, Experimental study of high-pressure turbulent premixed flames, Exp. Therm. Fluid Sci. 26 (2002) 375–387.
[30] Y.C. Chen, R.W. Bilger, Turbulence measurements on a bunsen burner inserted with perforated plugs of different hole sizes using DPIV, Exp. Therm. Fluid Sci. 27 (2003) 619–627.
[31] P. Griebel, P. Siewert, P. Jansohn, Flame characteristics of turbulent lean premixed methane/air flames at high pressure: Turbulent flame speed and flame brush thickness, Proc. Combust. Inst. 31 (2007) 3083–3090.
[32] E. Cintosun, G.J. Smallwood, Ö. L. Gülder, Flame surface fractal characteristics in premixed turbulent combustion at high turbulence intensities, AIAA J. 45 (2007) 2785–2789.
[33] F.T.C. Yuen, Ö. L. Gülder, Investigation of dynamics of lean turbulent premixed flames by Rayleigh imaging, AIAA J. 47 (2009) 2964–2973.
[34] F.T.C. Yuen, Ö. L. Gülder, Premixed turbulent flame front structure investigation by Rayleigh scattering in the thin reaction zone regime, Proc. Combust. Inst. 32 (2009) 1747–1754.
[35] F.T.C. Yuen, Ö. L. Gülder, Dynamics of lean-premixed turbulent combustion at high turbulence intensities, Combust. Sci. Technol. 182 (2010) 544–558.
[36] S. Kheirkhah, Ö. L. Gülder, Turbulent premixed combustion in V-shaped flames: Characteristics of flame front, Phys. Fluids 25 (2013) 055107.
[37] S. Kheirkhah, Ö. L. Gülder, Topology and brush thickness of turbulent premixed V-shaped flames, Flow Turbul. Combust. 93 (2014) 439–459.
[38] J. Mi, P. Kalt, G.J. Nathan, C.Y. Wong, PIV measurements of a turbulent jet issuing from round sharp-edged plate, Exp. Fluids 42 (2007) 625–637.
[39] P. Siewert, Flame Front Characteristics of Turbulent Lean Premixed Methane/Air Flames at High-pressure, ETH Zürich, 2006 (Ph.D. thesis).
[40] Y.C. Chen, N. Peters, G.A. Schneemann, N. Wruck, U. Renz, M.S. Mansour, The detailed flame structure of highly stretched turbulent premixed methane-air flames, Combust. Flame 107 (1996) 223–244.
[41] L.H. Benedict, R.D. Gould, Towards better uncertainty estimates for turbulence statistics, Exp. Fluids 22 (1996) 129–136.
[42] G.K. Batchelor, The Theory of Homogeneous Turbulence, Cambridge University Press, 1953.
[43] D. Goodwin, N. Malaya, H.K. Moffat, R. Speth, Cantera: An object-oriented software toolkit for chemical kinetics, thermodynamics, and transport processes. Available at http://code.google.com/p/cantera/.
[44] G.P. Smith, D.M. Golden, M. Frenklach, N.W. Moriarty, B. Eiteneer, M. Goldenberg, C.T. Bowman, R.K. Hanson, S. Song, W.C. Gardiner, V.V. Lissianski, Z. Qin, GRI-Mech 3.0. Available at http://www.me.berkeley.edu/gri_mech/.

[45] K.J. Bosschaart, L.P.H. de Goey, The laminar burning velocity of flames propagating in mixtures of hydrocarbons and air measured with the heat flux method, Combust. Flame 136 (2004) 261–269.

[46] R.C. Reid, J.M. Prausnitz, B.E. Poling, The Properties of Gases and Liquids, fourth ed., McGraw-Hill Companies, 1987.

[47] S.B. Pope, Turbulent Flows, Cambridge University Press, 2000.

[48] R. Borghi, On the structure and morphology of turbulent premixed flames, in: C. Casci, C. Bruno (Eds.), Recent Advances in Aerospace Sciences, Plenum Press, New York, 1985, pp. 117–138.

[49] J.B. Moss, Simultaneous measurements of concentration and velocity in an open premixed turbulent flame, Combust. Sci. Technol. 22 (1980) 119–129.

[50] I.G. Shepherd, J.B. Moss, Characteristic scales for density fluctuations in a turbulent premixed flame, Combust. Sci. Technol. 33 (1983) 231–243.

[51] R.K. Cheng, I.G. Shepherd, Intermittency and conditional velocities in premixed conical turbulent flames, Combust. Sci. Technol. 52 (1987) 353–375.

[52] G.J. Smallwood, Ö. L. Gülder, D.R. Snelling, B.M. Deschamps, I. Gökalp, Characterization of flame front surfaces in turbulent premixed methane/air combustion, Combust. Flame 101 (1995) 461–470.

[53] T. Lachaux, F. Halter, C. Chauveau, I. Gökalp, I.G. Shepherd, Flame front analysis of high-pressure turbulent lean premixed methane–air flames, Proc. Combust. Inst. 30 (2005) 819–826.

[54] C. Cohé, F. Halter, C. Chauveau, I. Gökalp, Ö. L. Gülder, Fractal characterisation of high-pressure and hydrogen-enriched CH$_4$–air turbulent premixed flames, Proc. Combust. Inst. 31 (2007) 1345–1352.

[55] C. Cohé, C. Chauveau, I. Gökalp, D.F. Kurtuluş, CO$_2$ addition and pressure effects on laminar and turbulent lean premixed CH$_4$ air flames, Proc. Combust. Inst. 32 (2009) 1803–1810.

[56] F. Halter, C. Chauveau, I. Gökalp, D. Veynante, Analysis of flame surface density measurements in turbulent premixed combustion, Combust. Flame 156 (2009) 657–664.

[57] I.G. Shepherd, R.K. Cheng, An experimental evaluation of the BLM model of the scalar field in turbulent premixed flames, Combust. Sci. Technol. 59 (1988) 341–353.

[58] R.K. Cheng, I.G. Shepherd, I. Gökalp, A comparison of the velocity and scalar spectra in premixed turbulent flames, Combust. Flame 78 (1989) 205–221.

[59] I.G. Shepherd, Flame surface density and burning rate in premixed turbulent flames, Proc. Combust. Inst. 26 (1996) 373–379.

[60] C.K. Chan, K.S. Lau, W.K. Chin, R.K. Cheng, Freely propagating open premixed turbulent flames stabilized by swirl, Proc. Combust. Inst. 24 (1992) 511–518.

[61] R.K. Cheng, Velocity and scalar characteristics of premixed turbulent flames stabilized by weak swirl, Combust. Flame 101 (1995) 1–14.

[62] A. Marshall, J. Lundrigan, P. Venkateswaran, J. Seitzman, T. Lieuwen, Fuel effects on leading point curvature statistics of high hydrogen content fuels, Proc. Combust. Inst. 35 (2015) 1417–1424.

[63] F.E. Hernández-Pérez, F.T.C. Yuen, C.P.T. Groth, Ö. L. Gülder, LES of a laboratory-scale turbulent premixed Bunsen flame using FSD, PCM-FPI and thickened flame models, Proc. Combust. Inst. 33 (2011) 1365–1371.

[64] F.E. Hernández-Pérez, Ö. L. Gülder, C.P.T. Groth, Large-eddy simulation of lean hydrogen–methane turbulent premixed flames in the methane-dominated regime, Int. J. Hydrogen Energy 39 (2014) 7147–7157.

[65] N. Shahbazian, M.M. Salehi, C.P.T. Groth, Ö. L. Gülder, W.K. Bushe, Performance of conditional source-term estimation model for LES of turbulent premixed flames in thin reaction zones regime, Proc. Combust. Inst. 35 (2015) 1367–1375.

[66] J.B. Bell, M.S. Day, J.F. Grcar, M.J. Lijewski, J.F. Driscoll, S.A. Filatyev, Numerical simulation of a laboratory-scale turbulent slot flame, Proc. Combust. Inst. 31 (2007) 1299–1307.

[67] A. Boukhalfa, I. Gökalp, Influence of the Damköhler number on the average thickness of conical turbulent premixed methane/air flames, Combust. Flame 73 (1988) 75–87.

[68] B. Deschamps, Étude spatiale et temporelle de la structure dynamique et scalaire des flammes turbulentes premelangees de méthane-air, University of Orléans, 1990 (Ph.D. thesis).

[69] M. Namazian, I.G. Shepherd, L. Talbot, Characterization of the density fluctuations in turbulent V-shaped premixed flames, Combust. Flame 64 (1986) 299–308.

[70] F.C. Gouldin, P.C. Miles, Chemical closure and burning rates in premixed turbulent flames, Combust. Flame 100 (1995) 202–210.

[71] G.G. Lee, K.Y. Huh, H. Kobayashi, Measurement and analysis of flame surface density for turbulent premixed combustion on a nozzle-type burner, Combust. Flame 122 (2000) 43–57.

[72] P. Venkateswaran, Measurements and Modeling of Turbulent Consumption Speeds of Syngas Fuel Blends, Georgia Institute of Technology, 2013 (Ph.D. thesis).

[73] F. Halter, C. Chauveau, I. Gökalp, Characterization of the effects of hydrogen addition in premixed methane/air flames, Int. J. Hydrogen Energy 32 (2007) 2585–2592.

[74] H. Kobayashi, H. Hagiwara, H. Kaneko, Y. Ogami, Effects of CO$_2$ dilution on turbulent premixed flames at high pressure and high temperature, Proc. Combust. Inst. 31 (2007) 1451–1458.

[75] M. Zhang, J. Wang, Y. Xie, Z. Wei, W. Jin, Z. Huang, H. Kobayashi, Measurement on instantaneous flame front structure of turbulent premixed CH$_4$/H$_2$/air flames, Exp. Therm. Fluid Sci. 52 (2014b) 288–296.

[76] M. Zhang, J. Wang, J. Wu, Z. Wei, Z. Huang, H. Kobayashi, Flame front structure of turbulent premixed flames of syngas oxyfuel mixtures, Int. J. Hydrogen Energy 39 (2014a) 5176–5185.

[77] M.Z. Haq, C.G.W. Sheppard, R. Woolley, D.A. Greenhalgh, R.D. Lockett, Wrinkling and curvature of laminar and turbulent premixed flames, Combust. Flame 131 (2002) 1–15.

[78] J. Kariuki, J.R. Dawson, E. Mastorakos, Measurements in turbulent premixed bluff body flames close to blow-off, Combust. Flame 159 (2012) 2589–2607.

[79] F. Mokhtarian, A. Mackworth, Scale-based description and recognition of planar curves and two-dimensional shapes, IEEE Pattern Anal. 8 (1986) 34–43.

[80] Y.C. Chen, Measurements of flame-front curvature based on Fourier transformation, Combust. Theor. Model. 11 (2007) 333–349.

[81] G. Troiani, F. Battista, F. Picano, Turbulent consumption speed via local dilatation rate measurements in a premixed bunsen jet, Combust. Flame 160 (2013) 2029–2037.

[82] I.G. Shepherd, R.K. Cheng, T. Plessing, C. Kortschik, N. Peters, Premixed flame front structure in intense turbulence, Proc. Combust. Inst. 29 (2002) 1833–1840.

[83] M. Day, S. Tachibana, J. Bell, M. Lijewski, V. Beckner, R.K. Cheng, A combined computational and experimental characterization of lean premixed turbulent low swirl laboratory flames: I. Methane flames, Combust. Flame 159 (2012) 275–290.

[84] A.E. Bayley, Y. Hardalupas, A.M.K.P. Taylor, Local curvature measurements of a lean, partially premixed swirl-stabilised flame, Exp. Fluids 52 (2012) 963–983.

[85] S. Gashi, J. Hult, K.W. Jenkins, N. Chakraborty, S. Cant, C.F. Kaminski, Curvature and wrinkling of premixed flame kernels—comparisons of OH PLIF and DNS data, Proc. Combust. Inst. 30 (2005) 809–817.

[86] L.W. Kostiuk, I.G. Shepherd, K.N.C. Bray, Experimental study of premixed turbulent combustion in opposed streams. Part III—spatial structure of flames, Combust. Flame 118 (1999) 129–139.

[87] F.T.C. Yuen, Ö. L. Gülder, Turbulent premixed flame front dynamics and implications for limits of flamelet hypothesis, Proc. Combust. Inst. 34 (2013) 1393–1400.

[88] Y.C. Chen, M. Kim, J. Han, S. Yun, Y. Yoon, Analysis of flame surface normal and curvature measured in turbulent premixed stagnation-point flames with crossed-plane tomography, Proc. Combust. Inst. 31 (2007) 1327–1335.

[89] J. Kerl, C. Lawn, F. Beyrau, Three-dimensional flame displacement speed and flame front curvature measurements using quad-plane PIV, Combust. Flame 160 (2013) 2757–2769.

[90] J. Wang, M. Zhang, Z. Huang, T. Kudo, H. Kobayashi, Measurement of the instantaneous flame front structure of syngas turbulent premixed flames at high pressure, Combust. Flame 160 (2013) 2434–2441.

[91] I.G. Shepherd, R.K. Cheng, The burning rate of premixed flames in moderate and intense turbulence, Combust. Flame 127 (2001) 2066–2075.

[92] S.B. Pope, The evolution of surfaces in turbulence, Int. J. Eng. Sci. 26 (1988) 445–469.

[93] A.M. Steinberg, J.F. Driscoll, S.L. Ceccio, Measurements of turbulent premixed flame dynamics using cinema stereoscopic PIV, Exp. Fluids 44 (2008) 985–999.

[94] G. Damköhler, Der Einfluß der Turbulenz auf die Flammengeschwindigkeit in Gasgemischen, Z. Electrochem. 46 (1940) 601–652.

[95] T.C. Chew, K.N.C. Bray, R.E. Britter, Spatially resolved flamelet statistics for reaction rate modeling, Combust. Flame 80 (1990) 65–82.

[96] B.M. Deschamps, G.J. Smallwood, J. Prieur, D.R. Snelling, Ö. L. Gülder, Surface density measurements of turbulent premixed flames in a spark-ignition engine and a bunsen-type burner using planar laser-induced fluorescence, Proc. Combust. Inst. 26 (1996) 427–435.

[97] Y.C. Chen, R.W. Bilger, Experimental investigation of three-dimensional flame-front structure in premixed turbulent combustion—I: hydrocarbon/air bunsen flames, Combust. Flame 131 (2002) 400–435.

[98] I.G. Shepherd, Wm.M. Ashurst, Flame front geometry in premixed turbulent flames, Proc. Combust. Inst. 24 (1992) 485–491.

[99] A. Trouvé, T. Poinsot, The evolution equation for the flame surface density in turbulent premixed combustion, J. Fluid Mech. 278 (1994) 1–31.

[100] Y.C. Chen, Measurements of three-dimensional mean flame surface area ratio in turbulent premixed Bunsen flames, Proc. Combust. Inst. 32 (2009) 1771–1777.

[101] P. Venkateswaran, A. Marshall, D.H. Shin, D. Noble, J. Seitzman, T. Lieuwen, Measurements and analysis of turbulent consumption speeds of H$_2$/CO mixtures, Combust. Flame 158 (2011) 1602–1614.

[102] P. Venkateswaran, A. Marshall, J. Seitzman, T. Lieuwen, Scaling turbulent flame speeds of negative Markstein length fuel blends using leading points concepts, Combust. Flame 162 (2015) 375–387.

[103] K. Herrmann, Strömung, flammencharakterisierung und stickoxid-bildung in turbulenten vormischflammen, ETH Zürich, 2002 (Ph.D. thesis).

[104] D.C. Haworth, T.J. Poinsot, Numerical simulations of Lewis number effects in turbulent premixed flames, J. Fluid Mech. 244 (1992) 405–436.

[105] J.B. Bell, M.S. Day, J.F. Grcar, Numerical simulation of premixed turbulent methane combustion, Proc. Combust. Inst. 29 (2002) 1987–1993.

[106] E.R. Hawkes, J.H. Chen, Comparison of direct numerical simulation of lean premixed methane–air flames with strained laminar flame calculations, Combust. Flame 144 (2006) 112–125.

[107] Y.C. Lin, P. Jansohn, K. Boulouchos, Turbulent flame speed for hydrogen-rich fuel gases at gas turbine relevant conditions, Int. J. Hydrogen Energy 39 (2014) 20242–20254.